



HAL
open science

Modulation of Wind-Work by Oceanic Current Interaction with the Atmosphere

Lionel Renault, M. Jeroen Molemaker, James C. McWilliams, Alexander Shchepetkin, Florian Lemarié, Dudley Chelton, Serena Illig, Alex Hall

► **To cite this version:**

Lionel Renault, M. Jeroen Molemaker, James C. McWilliams, Alexander Shchepetkin, Florian Lemarié, et al.. Modulation of Wind-Work by Oceanic Current Interaction with the Atmosphere. *Journal of Physical Oceanography*, 2016, 46 (6), pp.1685-1704. 10.1175/JPO-D-15-0232.1 . hal-01295496

HAL Id: hal-01295496

<https://inria.hal.science/hal-01295496>

Submitted on 31 Mar 2016

HAL is a multi-disciplinary open access archive for the deposit and dissemination of scientific research documents, whether they are published or not. The documents may come from teaching and research institutions in France or abroad, or from public or private research centers.

L'archive ouverte pluridisciplinaire **HAL**, est destinée au dépôt et à la diffusion de documents scientifiques de niveau recherche, publiés ou non, émanant des établissements d'enseignement et de recherche français ou étrangers, des laboratoires publics ou privés.

1 **Modulation of Wind-Work by Oceanic Current Interaction with**
2 **the Atmosphere**

3 LIONEL RENAULT^{(1)*}, Jeroen Molemaker⁽¹⁾, James C. McWilliams⁽¹⁾,
Alexander F. Shchepetkin⁽¹⁾, Florian Lemarié⁽²⁾,
Dudley Chelton⁽³⁾, Serena Illig⁽⁴⁾, Alex Hall⁽¹⁾

(1) Department of Atmospheric and Oceanic Sciences, University of California, Los Angeles, California, USA

(2) INRIA, Univ. Grenoble-Alpes, CNRS, LJK, F-38000 Grenoble, France

(3) College of Earth, Ocean, and Atmospheric Sciences, Oregon State University, Oregon, USA

(4) Laboratoire d'Étude en Géophysique et Océanographie Spatiale, IRD, Toulouse, France

* *Corresponding author address:* Lionel Renault, Department of Atmospheric and Oceanic Sciences, University of California, Los Angeles, 405 Hilgard Ave., Los Angeles, CA 90095-1565.

E-mail: lrenault@atmos.ucla.edu

ABSTRACT

4
5 In this study, uncoupled and coupled ocean-atmosphere simulations are carried out over the
6 California Upwelling System to assess the dynamic ocean-atmosphere interactions, *viz.*, the
7 ocean surface current feedback to the atmosphere. We show the current feedback, by mod-
8 ulating the energy transfer from the atmosphere to the ocean, controls the oceanic Eddy
9 Kinetic Energy (EKE), and for the first time, we demonstrate the current feedback has an
10 opposite effect on the surface stress and on the wind itself. The current feedback acts as
11 an oceanic eddy killer, reducing by half the Surface EKE, and by 27% the depth-integrated
12 EKE. On one hand, it reduces the coastal generation of eddies by weakening the nearshore
13 supply of positive wind work. On the other hand, offshore, it removes energy from the
14 geostrophic current into the atmosphere, damping eddies. A negative feedback on the sur-
15 face stress explains the coastal reduction of energy transfer from the atmosphere to the ocean
16 and an offshore return of energy from the ocean to the atmosphere, partially re-energizing the
17 atmosphere. This, in turn, partly re-energizes the ocean by increasing the coastal transfer of
18 energy from the atmosphere and by inducing an opposite wind curl, decreasing the offshore
19 return of energy to the atmosphere. Eddy statistics confirm the current feedback damps
20 the eddies and reduces their lifetime, improving the realism of the simulation. Finally, we
21 propose an additional energy element in the Lorenz diagram of energy conversion, *viz.*, the
22 current-induced transfer of energy from the ocean to the atmosphere at the eddy scale.

1. Introduction

Eastern Boundary Upwelling Systems (EBUS), such as the California Current System (CCS), belong to the most productive coastal environments (*e.g.*, Carr and Kearns 2003), supporting some of the world’s major fisheries (*e.g.*, FAO 2009). The CCS upwelling and productivity present a seasonal variability with a favorable season during spring and summer (Marchesiello et al. 2003, Renault et al. 2015b), where high biological productivity is largely determined by wind-driven upwelling. As for the other EBUS (*e.g.*, Benguela, Canary and Humboldt), equatorward winds drive coastal upwelling, Ekman pumping, alongshore currents and then productivity. Additionally, coastal currents and significant oceanic mesoscale variability contribute to cross-shore exchange of heat, salt, and biogeochemical tracers between the open and coastal oceans (Marchesiello et al. 2003, Capet et al. 2008b, Gruber et al. 2011, Chaigneau et al. 2011).

Eddies generated by dynamical instabilities of the currents (Marchesiello et al. 2003) lead to lateral heat transport, so that effects of coastal upwelling on Sea Surface Temperature (SST) can be felt hundreds of km away (Capet et al. 2008b). In the open ocean, and in particular in low-nutrient environments, mesoscale processes increase the net upward flux of limiting nutrients and enhance biological production (Martin and Richards 2001; McGillicuddy et al. 2007). For the EBUS, as shown by *e.g.*, Carr and Kearns (2003), the Net Primary Production (NPP) is primarily controlled by the magnitude of the upwelling favorable winds through the upwelling strength. However, Lathuilière et al. (2010), Gruber et al. (2011), and Renault et al. (2015a) also show that eddies can be a limiting factor, which progressively prevent high levels of NPP as the number of eddies increase by subducting the

45 nutrient below the euphotic layer ("eddy quenching"). Renault et al. (2015a) show that the
46 coastal wind shape, by modulating the baroclinic instabilities, modulates the Eddy Kinetic
47 Energy (EKE) and therefore the eddy quenching. The eddy contribution to oceanic fluxes
48 is substantial (Colas et al. 2013), and a realistic wind forcing is crucial to simulate the
49 mesoscale activity realistically (Renault et al. 2015a).

50 In the EBUS, various processes can modulate the spatial pattern of the wind, *e.g.*, sharp
51 changes of surface drag and atmospheric boundary layer at the land-sea interface (Edwards
52 et al. 2001, Capet et al. 2004, Renault et al. 2015b), coastal orography (Edwards et al. 2001,
53 Perlin et al. 2011, Renault et al. 2015b), and SST-wind coupling (Chelton et al. 2007, Jin
54 et al. 2009). Renault et al. 2015b and Renault et al. 2015a show that the coastal wind
55 shape in the CCS is mainly controlled by the orography. These coastal circulation processes
56 are essential for understanding the upwelling systems (Marchesiello et al. 2003, Capet et al.
57 2004, Renault et al. 2012). The ocean feedback to the atmosphere has been recently studied,
58 mainly focusing on the thermal feedback (*e.g.*, Chelton et al. 2004, Chelton et al. 2007, Spall
59 2007, Perlin et al. 2007, 2011, Minobe et al. 2008, Jin et al. 2009, Park et al. 2006, Cornillon
60 and Park 2001). SST gradients induce gradients in lower-atmospheric stratification; hence,
61 gradients in vertical momentum flux in the atmospheric boundary layer and gradients in the
62 surface wind and stress are induced beneath an otherwise more uniform mid-tropospheric
63 wind. Chelton et al. (2004) and Chelton et al. (2007), using satellite observations, show
64 approximately linear relationships between the surface stress curl and divergence and the
65 crosswind and downwind components of the local SST gradient. Recent studies also highlight
66 how a mesoscale SST front may have an impact up to the troposphere (Minobe et al. 2008).
67 The effect of oceanic currents is another aspect of interaction between atmosphere and ocean;

68 however, its effects are not yet well known. Some work shows that the current effect on the
69 surface stress can lead to a reduction of the EKE of the ocean via a "mechanical damping"
70 (Duhaut and Straub 2006; Dewar and Flierl 1987; Dawe and Thompson 2006; Hughes and
71 Wilson 2008; Eden and Dietze 2009) and hence a reduction of the wind work. However,
72 in those studies the atmospheric response to the current feedback is neglected. Recently,
73 Seo et al. (2015), using coupled model, confirms the current feedback induces a reduction
74 of the wind work, that in turn, damps the EKE. To our knowledge, the effects of surface
75 currents on the surface wind speed has not been yet studied. Eden and Dietze (2009) can be
76 associated with an observational analysis that shows that the current-induced surface stress
77 curl change induces Ekman pumping velocities that are of the opposite sign to the surface
78 vorticity of the eddy, inducing its attenuation (Gaube et al. 2015).

79 In oceanic numerical modeling, the surface stress is usually estimated as a function of
80 the wind speed, ignoring the fact that the current also has a drag force on the atmosphere.
81 Scott and Xu (2009) shows such a simplification can lead to an overestimation of the total
82 energy input to the ocean by wind work and suggests the current should be included when
83 estimating the surface stress. In this paper, using a set of coupled and partially coupled
84 simulations, the focus is on this surface current feedback to the atmosphere. The objectives
85 are to assess how the current feedback modifies the wind work and to address how it alters
86 both the atmospheric and oceanic EKE. This raises the question of how best to force an
87 oceanic model. Oceanic simulations forced by a prescribed wind stress inherently cannot
88 represent the current feedback on the stress. Furthermore, although uncoupled oceanic
89 simulations forced by an atmospheric wind product can estimate the surface stress using
90 the air-sea velocity difference, they cannot represent the influence of surface currents on the

91 surface wind speed, to our knowledge, this point has not previously been documented

92 The paper is organized as follows: Section 2 describes the model configuration and
93 methodology. In Sec. 3, the effect of the current feedback on the surface stress and EKE is
94 assessed. Section 4 addresses the corresponding wind adjustment. In Sec. 5 an eddy attenu-
95 ation time scale and Ekman pumping are estimated, and a mechanistic view of the current
96 feedback effect is presented. In Sec. 6 an eddy statistical view allows a direct validation
97 of our results by comparison to observations. The results are discussed in Sec. 7, which is
98 followed by the conclusions.

99 **2. Model Configuration and Methodology**

100 *a. The Regional Oceanic Modeling System (ROMS)*

101 The oceanic simulations were performed with the Regional Oceanic Modeling System
102 (ROMS) (Shchepetkin and McWilliams 2005) in its AGRIF (Adapted Grid Refinement in
103 Fortran) version) (Debreu et al. 2012). ROMS is a free-surface, terrain-following coordinate
104 model with split-explicit time stepping and Boussinesq and hydrostatic approximations.
105 ROMS is implemented in a configuration with two offline nested grids. The coarser grid
106 extends from 170°W to 104°W and from 18°N to 62.3°N along the U.S. West Coast and is
107 322 x 450 points with a resolution of 12 km. Its purpose is to force the second domain. The
108 second domain grid extends from 144.7°W to 112.5°W and from 22.7°N to 51.1°N (Fig. 1).
109 The model grid is 437 x 662 points with a resolution of 4 km. The boundary condition
110 algorithm consists of a modified Flather-type scheme for the barotropic mode (Mason et al.

111 2010) and Orlanski-type scheme for the baroclinic mode (including T and S; Marchesiello
112 et al. 2001).

113 Bathymetry for all domains is constructed from the Shuttle Radar Topography Mission
114 (SRTM30 plus) dataset (available online at <http://topex.ucsd.edu/WWW.html/srtm30plus.html>)
115 based on the 1-min Sandwell and Smith (1997) global dataset and higher-resolution data
116 where available. A Gaussian smoothing kernel with a width of 4 times the topographic grid
117 spacing is used to avoid aliasing whenever the topographic data are available at higher res-
118 olution than the computational grid and to ensure the smoothness of the topography at the
119 grid scale. The slope parameter ($r = \Delta h / 2\bar{h}$) is a ratio of the maximum difference between
120 adjacent grid cell depths and the mean depth at that point, used to assess the potential im-
121 pact of errors induced by terrain-following (s-coordinate) horizontal layers. In regions with
122 steep terrain combined with shallow depths, a relatively small r_{max} is necessary to prevent
123 pressure gradient errors which result in artificial currents developing from a state of rest
124 with no forcing (Beckmann and Haidvogel 1993) Here, local smoothing is applied where the
125 steepness of the topography exceeds a factor $r_{max} = 0.2$.

126 Lateral oceanic forcing for the largest domain as well as surface forcing for all simulations
127 are interannual. Temperature, salinity, surface elevation, and horizontal velocity initial and
128 boundary information for the largest domain covering the whole North America West Coast
129 are taken from the monthly averaged Simple Ocean Data Assimilation (SODA) ocean inter-
130 annual outputs (Carton and Giese 2008). A bulk formulae (Large 2006) is used to estimate
131 the freshwater, turbulent, and momentum fluxes using the atmospheric fields derived from
132 the uncoupled WRF simulation. In the coupled simulations, the fluxes are computed by
133 WRF and then given to ROMS using the same bulk formulae.

134 The 12 km domain is first spun up from the SODA initial state the 1st January 1994 for a
135 few months, then run for an additional period until end of 1999. Kinetic energy in the domain
136 is statistically equilibrated within the first few months of simulation. The second grid (4 km
137 resolution) is then nested in the parent grid from 1st June 1994. Results obtained after a
138 6-month spin-up are then used in our analysis. All domains have 42 levels in the vertical
139 with the same vertical grid system concentrating vertical levels near the surface (Shchepetkin
140 and McWilliams 2009), with stretching surface and bottoms parameters $hcline = 250 m$,
141 $\theta b = 1.5$, and $thetas = 6.5$. Finally, vertical mixing of tracers and momentum is done
142 with a K-profile parameterization (KPP; Large et al. 1994). In this study, only the period
143 1995-1999 is analyzed.

144 *b. The Weather Research and Forecast (WRF) Model*

145 WRF (version 3.6, Skamarock et al. 2008) is implemented in a configuration with two
146 nested grids. The largest domain covers the North American West Coast with a horizontal
147 resolution of 18 km (not shown); the inner domain covers the U.S. West Coast, with a
148 horizontal resolution of 6 km (see Renault et al. 2015b), that is slightly larger than the
149 ROMS 4 km grid. The coarser grid (WRF18) reproduces the large-scale synoptic features
150 that force the local dynamics in the second grid, each using a one-way offline nesting with
151 three-hourly updates of the boundary conditions. The coarser grid simulation (WRF18) was
152 first run independently. It is initialized with the Climate Forecast System Reanalysis (CFSR)
153 ($\approx 40 km$ spatial resolution; Saha et al. 2010) from 1st January 1994 and integrated for 6
154 years with time-dependent boundary conditions interpolated from the same three-hourly

155 reanalysis. Forty vertical levels are used, with half of them in the lowest 1.5 km. The nested
156 domain (WRF6) was initialized from the coarse solution WRF18 on 1rd June 1994 and
157 integrated 5.5 years.

158 A full set of parameterization schemes is included in WRF. The model configuration was
159 setup with the following parameterizations: the WRF Single-Moment 6-class microphysics
160 scheme (Hong and Lim 2006) modified to take into account the droplet concentration (Jousse
161 et al. 2015); the Tiedtke cumulus parameterization (Zhang et al. 2011); the new Goddard
162 scheme for shortwave and longwave radiation (Chou and Suarez 1999) the Noah land surface
163 model (Skamarock et al. 2008); and the MYNN2.5 planetary boundary layer (PBL) scheme
164 (Nakanishi and Niino 2006).¹

165 *c. OASIS/MCT Coupling Procedure*

166 The OASIS coupler ([https://verc.enes.org/oasis/
167 metrics/oasis4-dissemination](https://verc.enes.org/oasis/metrics/oasis4-dissemination)), which is based on MCT (Model Coupling Toolkit; devel-
168 oped at Argonne National Lab) and supports exchanges of general two-dimensional fields
169 between numerical codes representing different components of the climate system. All trans-
170 formations, including regridding, are executed in parallel on the set of source or target
171 component processes, and all coupling exchanges are executed in parallel directly between
172 the components. In our configuration, every hour, WRF gives to ROMS the hourly averages
173 of freshwater, heat, and momentum fluxes, whereas ROMS sends to WRF the hourly SST

¹Other WRF PBL schemes were tried (*e.g.*, Yonsei University YSU, (Hong et al. 2006), University of Washington, Park and Bretherton (2009)). The MYNN2.5 gave in general more realistic features, especially in terms of cloud cover.

174 and eventually, the surface currents.

175 *d. Experiments*

176 Table 1 summarizes the three experiments carried out to assess the impact of the oceanic
177 currents on the surface stress, the wind, and the oceanic EKE. EXP1 is a SST coupled
178 ROMS-WRF simulation. EXP2 is an uncoupled simulation that uses the atmosphere from
179 EXP1 and that takes into account the oceanic surface current when estimating the surface
180 stress. It allows us to assess the oceanic response to the current feedback. Finally, EXP3
181 is a fully coupled simulation in the sense that it has both thermal and current feedbacks to
182 the atmosphere. The surface stress is estimated using a bulk formula with a velocity that is
183 the wind relative to the current:

$$\mathbf{U} = \mathbf{U}_a - \mathbf{U}_o, \quad (1)$$

184 where \mathbf{U}_a and \mathbf{U}_o are the surface wind (at the first vertical level in WRF) and the surface
185 current, respectively. As described by Lemarié (2015), because of the implicit treatment
186 of the bottom boundary condition in most atmospheric models, the use of relative winds
187 involves a modification of both the surface-layer vertical mixing parameterization (MYNN2.5
188 in our case) and the tridiagonal matrix for vertical turbulent diffusion.

189 *e. EKE Budget*

190 All quantities are decomposed into a 1995-1999 time mean (overbar, "̄") and deviations
191 (primes, "'"). In our analysis the seasonal variability is not removed.

192 The total wind work is defined as

$$FK = \frac{1}{\rho_0} (\overline{\tau_x u_o} + \overline{\tau_y v_o}), \quad (2)$$

193 where u_o and v_o are the zonal and meridional surface currents, τ_x and τ_y are the zonal and
 194 meridional surface stresses, and ρ_0 is mean seawater density.

195 The geostrophic wind work is defined as

$$FK_g = \frac{1}{\rho_0} (\overline{\tau_x u_{og}} + \overline{\tau_y v_{og}}), \quad (3)$$

196 where u_{og} and v_{og} are the zonal and meridional surface geostrophic currents.

197 As in Marchesiello et al. (2003), we focus on the following relevant energy source and
 198 eddy-mean conversion terms:

199 • The mean wind work:

$$F_m K_m = \frac{1}{\rho_0} (\overline{\tau_x u_o} + \overline{\tau_y v_o}). \quad (4)$$

200 • The eddy wind work:

$$F_e K_e = \frac{1}{\rho_0} (\overline{\tau'_x u'_o} + \overline{\tau'_y v'_o}). \quad (5)$$

201 • Barotropic (Reynolds stress) conversion $K_m K_e$:

$$K_m K_e = \int_z -(\overline{u'_o u'_o} \frac{\partial \overline{u_o}}{\partial x} + \overline{u'_o v'_o} \frac{\partial \overline{u_o}}{\partial y} + \overline{u'_o w'} \frac{\partial \overline{u_o}}{\partial z} + \overline{v'_o u'_o} \frac{\partial \overline{v_o}}{\partial x} + \overline{v'_o v'_o} \frac{\partial \overline{v_o}}{\partial y} + \overline{v'_o w'} \frac{\partial \overline{v_o}}{\partial z}), \quad (6)$$

202 where w is the vertical velocity and x , y , and z are the zonal, meridional, and vertical
 203 coordinates, respectively.

204 • Baroclinic conversion $P_e K_e$:

$$P_e K_e = \int_z -\frac{g}{\rho_0} \overline{\rho' w'}, \quad (7)$$

205 where g is the gravitational acceleration.

206 $F_m K_m$ represents the transfer of energy from mean surface wind-forcing to mean Kinetic
207 Energy, $F_e K_e$ represents the transfer of energy from surface wind-forcing anomalies to EKE,
208 $K_m K_e$ represents the barotropic conversion from mean kinetic energy to EKE, and $PeKe$
209 represents the baroclinic conversion from eddy available potential energy to EKE. We com-
210 puted those conversion terms at each model grid point. The anomalies are estimated with
211 respect to the long-term means. The wind work is estimated at the free surface, whereas the
212 barotropic and baroclinic conversion terms are integrated over the whole water column. In
213 the following, cross-shore sections are evaluated using d as the cross-shore distance.

214 *f. Eddy Tracking*

215 The eddy tracking detection method developed by Chelton et al. (2011) is used to detect
216 and track eddies in the simulations and in the AVISO dataset (Ducet et al. 2000). This
217 approach consists of detecting closed contours of Sea Level Anomalies (SLA) that include a
218 local extremum and several other criteria to identify and track mesoscale eddies. An eddy
219 is viewed as a coherent isolated vortex and therefore the corresponding SLA has the form of
220 a bump or a depression. Before applying the eddy tracking procedure, the model outputs
221 were first filtered by removing the seasonal cycle (annual plus semiannual components) at
222 each grid point. In this study, we define the long-lived eddies as tracked eddies that have a
223 continuous lifetime greater than 16 weeks. The AVISO data are only able to resolve eddies
224 with radii longer than about 40 km (Chelton et al. 2011). However, although the eddy
225 lifetime dependence on eddy scale in the real ocean is not yet known, by focusing on eddies
226 with long lifetimes, the resolution capability of the AVISO dataset should not be a major

227 limitation.

228 **3. Eddy Kinetic Energy and Energy Conversion**

229 *a. Eddy Kinetic Energy*

230 The surface EKE from the different experiments is estimated using the daily surface
231 current perturbations. The mean surface EKE and the temporal evolution of its domain-
232 average are in Fig. 1. In good agreement with the literature (Marchesiello et al. 2003;
233 Renault et al. 2015a), in all the experiments the EKE has larger values not too far offshore
234 and exhibits a broad decay further offshore. EXP1 shows a relatively weak decay with
235 high values of EKE offshore. From EXP1 to EXP2, the current feedback to the surface
236 stress reduces the EKE by 55%, and in particular, it strongly decreases the offshore EKE,
237 improving the realism of the simulation (*e.g.*, see Fig. 2 from Capet et al. 2008a). EXP3 also
238 reduces the surface EKE relative to EXP1, but only by 40%, which is in good agreement with
239 Seo et al. 2015. The atmospheric response to the reduced wind work with current feedback
240 leads to an increase in surface wind strength (see Section 4b), hence the EKE reduction
241 observed in EXP2 is diminished. To our knowledge, this is the first time this phenomenon
242 has been documented. Similar conclusions can be drawn using the depth-integrated EKE:
243 from EXP1 to EXP2, it is reduced by 35%, whereas, from EXP1 to EXP3, it is reduced by
244 only 27 %. The exclusion of an atmospheric response in EXP2 leads to an overestimation of
245 the oceanic EKE reduction, both nearshore and offshore. The EKE reduction can be split
246 into two processes. On one hand, there is a surface stress adjustment that tends to reduce

247 the EKE (EXP2). On the other hand, there is a wind adjustment that partly counteracts
248 the surface stress reduction, thus attenuating the EKE reduction (EXP3).

249 *b. Energy Conversion*

250 A simplified EKE budget (Sec. 2e) is computed to diagnose which processes lead to the
251 EKE reduction by the current feedback. Since the time-mean quantities and then $F_m K_m$
252 are barely affected by the current feedback (about 1% change, not shown), Fig. 2 shows
253 the spatial distribution of only $F_e K_e$, $P_e K_e$, and $K_m K_e$ from EXP1 (top panel) and EXP3
254 (bottom panel), and Fig. 3 is the cross-shore profile for each term averaged between 30°N
255 and 45°N from EXP1, EXP2, and EXP3. As in Marchesiello et al. (2003), the baroclinic
256 instability and the eddy wind work are the main sources of EKE, and they have higher
257 values in the nearshore region. Note, here, that $K_m K_e$ is a secondary term. The wind
258 work is also stronger in those simulations than in Marchesiello et al. (2003), which can be
259 attributed to the poor quality of the wind used in Marchesiello et al. (2003) (*i.e.*, COADS):
260 it is monthly, and in particular it does not resolve the high frequency wind forcing (hourly
261 here, which excites inertial currents) nor the slackening of the winds near the coast (drop-off,
262 *e.g.*, Renault et al. 2015a). The COADS wind stress forcing induces too low levels of EKE.
263 As in Marchesiello et al. (2003), in the nearshore region, a coastal band of about 80 km
264 width is marked by a large values of $F_e K_e$. In all the experiments, the wind perturbations
265 induce an offshore Ekman surface current and an oceanic coastal jet (*e.g.*, Renault et al.
266 2009) that flows partly in the same direction as the wind, inducing a positive $F_e K_e$. Also
267 offshore, the Ekman surface current is partly in the direction of the wind with a generally

268 positive $F_e K_e$.

269 The main effect of the current feedback is a reduction of $F_e K_e$ in both the nearshore
270 and offshore regions (Figs. 2 and 3). The oceanic surface current can be split into their
271 geostrophic and ageostrophic parts:

$$u_o = u_{og} + u_{oa} \quad (8)$$

272 and

$$v_o = v_{og} + v_{oa}, \quad (9)$$

273 with u_{og} , v_{og} , u_{oa} , and v_{oa} the zonal and meridional geostrophic and ageostrophic currents,
274 respectively. Using (8) and (9), $F_e K_e$ can in turn be split into its geostrophic ($F_e K_{eg}$) and
275 ageostrophic ($F_e K_{ea}$) parts:

$$F_e K_{eg} = \frac{1}{\rho_0} (\overline{\tau'_x u'_{og}} + \overline{\tau'_y v'_{og}}) \quad (10)$$

276 and

$$F_e K_{ea} = \frac{1}{\rho_0} (\overline{\tau'_x u'_{oa}} + \overline{\tau'_y v'_{oa}}). \quad (11)$$

277 Figure 4 shows $F_e K_{eg}$ from EXP1 and EXP3, and Fig. 3c shows the cross-shore profile of
278 $F_e K_{eg}$ from EXP1, EXP2, and EXP3. In all the experiments, the offshore positive $F_e K_e$ is
279 essentially due to $F_e K_{ea}$ (more than 95%), whereas, nearshore, $F_e K_{ea}$ accounts for only 37%
280 of $F_e K_e$.

281 The induced current feedback reduction of $F_e K_e$ mainly acts through the geostrophic
282 currents. Offshore, the current-induced reduction of $F_e K_e$ is due to two different mechanisms:
283 1) a slight reduction of its ageostrophic part $F_e K_{ea}$ (3%; Fig. 3), that is explained by changes
284 in Ekman induced surface current. 2) a sink of energy through its geostrophic part $F_e K_{eg}$

285 (actual negative values of $F_e K_{eg}$). In that sense the current feedback acts as an “eddy
 286 killer”. Figure 5 illustrates the geostrophic sink through $F_e K_{eg}$ for an anticyclonic eddy
 287 with a southward uniform wind blowing up over such an eddy. In EXP1, over such an eddy,
 288 $F_e K_{eg}$ is equal to zero. There is a positive $F_e K_{eg}$ on the eastern branch and a negative
 289 $F_e K_{eg}$ on the western branch, with a uniform wind, the net $F_e K_{eg}$ is zero. In EXP2, the
 290 wind is still uniform since it does not react to the current feedback. However, the eastern
 291 branch has the currents acting in the same direction as the wind, and hence has a reduced
 292 surface stress, $\tau = C_d \rho_a (U_a - U_o)^2 < C_d \rho_a (U_a)^2$ (C_d is the drag coefficient), whereas the
 293 western branch has the currents acting against the wind, and hence an increased surface
 294 stress, $\tau = C_d \rho_a (U_a - U_o)^2 > C_d \rho_a U_a^2$. As a result, the positive (negative) part of $F_e K_{eg}$ is
 295 reduced (increased), and the net $F_e K_{eg}$ becomes negative, deflecting energy from the ocean
 296 to the atmosphere. In EXP3, the current feedback not only acts on the surface stress but also
 297 on the atmosphere and, in particular on the wind. The wind response damps the efficiency of
 298 the $F_e K_{eg}$ sink, explaining the damping of the offshore EKE reduction from EXP2 to EXP3
 299 shown in Fig. 1. On the eastern branch of the eddy, there is less friction and more energy
 300 in the atmosphere, so that the wind can accelerate, increasing the relative wind and hence
 301 increasing back $F_e K_{eg}$. On the western branch, there is more friction, that leads to a decrease
 302 of the wind, but also more energy, that should lead to an increase of the wind. On average,
 303 as shown in Sec. 4, it leads to a decrease of the wind and hence to a less negative $F_e K_{eg}$.
 304 The net $F_e K_{eg}$ in EXP3 is still negative but less than EXP2, the atmospheric response tends
 305 to re-energize the ocean.

306 In the coastal band of 80 km width, there is a reduction of energy input through $F_e K_{eg}$.
 307 As for the offshore region, the presence of eddies weakens the wind work. However, the wind

308 perturbations also induce an oceanic geostrophic coastal jet that blows partially toward the
 309 same direction as the wind. Hence, the relative wind $U = U_a - U_o$ taken into account to
 310 estimate the surface stress in EXP2 and EXP3 is weaker than the absolute wind U_a used in
 311 EXP1 to estimate the stress. As a result the stress perturbations are reduced in EXP2 and
 312 EXP3 with respect to EXP1, reducing $F_e K_{eg}$ (Fig. 6). In EXP3, as for the offshore region,
 313 the atmospheric response damps the current-induced surface stress reduction by changing
 314 the wind (Fig. 5 and . 6).

315 To sum up, although the atmospheric response tends to re-energize the ocean, the current
 316 feedback to the atmosphere acts as an eddy killer and induces an energy sink from the ocean
 317 to the atmosphere. Although the $F_e K_e$ sink of energy should be less effective in EXP3
 318 compared to EXP2, Fig. 3 shows that the offshore $F_e K_{eg}$ in EXP3 is only slightly larger
 319 than the one in EXP2. In EXP3, more EKE is generated in the coastal region that then
 320 propagates offshore. As a result there is a larger offshore energetic reservoir, and therefore
 321 a larger $F_e K_{eg}$ sink.

322 A co-spectrum analysis of the total wind work FK and its geostrophic part (FK_g) is
 323 performed point-wise for the coastal ($30^\circ - 45^\circ\text{N} \times d \leq 80 \text{ km}$) and offshore regions ($d > 80 \text{ km}$
 324 $\times 30^\circ\text{N} - \text{ and } 45^\circ\text{N}$) (Fig. 7).

325 $F_e K_e$ and $F_e K_{eg}$ both show large positive energy input at the low end of the frequency
 326 range that are mostly represent the annual cycle of winds acting on the mean California
 327 current and surface Ekman velocity. The focus of this study is fairly tiny perturbations
 328 from this dominant process that induce a damping of the EKE. Consistent with the previous
 329 results, in the coastal region the current feedback to the surface stress reduces the amount of
 330 energy input into the ocean between the frequencies 30-days^{-1} and 300-days^{-1} (not shown).

331 More interestingly, as illustrated in Fig. 7 using EXP1 and EXP3, offshore between 30-days^{-1}
 332 and 300-days^{-1} , there is a clear FK reduction due to a sink of FK_g , which leads to a transfer
 333 of energy from the ocean to the atmosphere. The sink of energy from the geostrophic currents
 334 to the atmosphere within the eddy scale band confirms that the current feedback acts as an
 335 “eddy killer”. As a result, the eddies decay as they propagate offshore and, therefore, are
 336 eventually very weak (or absent) very far offshore, explaining the offshore decay of EKE in
 337 Fig. 1. Thus, there is a route of energy from the atmosphere to the ocean in the nearshore
 338 region, offshore eddy propagation, and then from the offshore eddies to the atmosphere.
 339 Finally, in our analysis, the seasonal variability is not removed. At seasonal timescale, the
 340 wind has roughly the same direction than the surface currents, so that there is a seasonal
 341 positive geostrophic $F_e K_e$. The same analysis done without the seasonal variability, lead
 342 qualitatively to the same results, but with a slightly larger negative $F_e K_{eg}$ offshore (by
 343 5%). The large values of positive $F_e K_e$ in the nearshore region are also partly driven by the
 344 seasonal variability that represents about 30% of the coastal positive $F_e K_e$ (about 30%)..

345 4. Surface Stress and Wind Response

346 As reported by Chelton et al. (2007), the link between SST and wind stress in the
 347 California upwelling system exhibits a linear relationship between the wind stress curl and
 348 the crosswind SST gradient. EXP1 has a wind stress curl - crosswind SST gradient slope
 349 of $s_t = 0.019 m^2 C^{-1}$ for the summer season, that is similar to the one reported by Chelton
 350 et al. (2007). Similar values are found for the other experiments. Here, the focus is on an
 351 analogous linear relationship between the surface stress and the oceanic currents, and on the

352 influence of surface currents on the surface wind speed as apparently not previously been
353 documented.

354 *a. Current-Induced Surface Stress*

355 Similar to Chelton et al. (2007), the statistical relationship between surface stress curl
356 and oceanic current vorticity is evaluated by bin averaging the 1-month running means of
357 the stress curl as a function of the 1-month running means of the oceanic current vorticity
358 over the full simulated period for the three experiments. Bin sizes of 1 m s^{-1} per 100 km and
359 1 Nm^{-2} per 10^5 km are used for surface current vorticity and the stress curl, respectively.
360 The large scale signal is removed using a high-pass Gaussian spatial filter with a 150 km
361 cut-off. The analysis domain is $30^\circ \text{N} - 45^\circ \text{N}$ and $(150 \text{ km} < d < 500 \text{ km})$, *i.e.*, offshore
362 of the wind drop-off region, where the current feedback effects are partly masked by the
363 orographic, coastline, and SST effects on the wind (Perlin et al. 2011; Renault et al. 2015b).

364 Figure 8 shows the resulting scatterplots. A coupling correlation coefficient $s_{st} [\text{N s m}^{-3}]$
365 is defined as the slope of the linear regression in this scatterplot. Because EXP1 does not
366 consider the surface currents into its surface stress estimate, its wind stress curl does not
367 show any significant dependence on the oceanic vorticity. EXP2 and EXP3 show a clear neg-
368 ative linear relationship between the surface currents vorticity and the surface stress curl,
369 with $s_{st} < 0$. The negative sign is consistent with the $F_e K_{eg}$ sink and Fig. 5, *i.e.*, the current
370 feedback induces an opposite sign surface stress curl. From EXP2 to EXP3 the magnitude
371 of s_{st} decreases significantly. The difference is due to the atmospheric response of an in-
372 tensification of the surface wind that attenuates the current feedback effect on the surface

373 stress. Simulations that neglect the wind adjustment to the current feedback (*e.g.*, EXP2
374 and the North Atlantic simulations of Eden and Dietze (2009)) overestimate the reduction
375 of the surface stress by the oceanic surface currents, missing the partial re-energization of
376 both the atmosphere and ocean through full coupling.

377 *b. Wind Response*

378 The oceanic surface currents partially drive the atmosphere. When coupling the atmo-
379 sphere to the oceanic currents, the reduction in air-sea velocity difference reduces the stress
380 acting on the wind and allows it to accelerate. Figure 9 depicts the mean cross-shore profiles
381 of surface wind Turbulent Kinetic Energy (TKE) 30°N and 45°N. TKE is always larger in
382 EXP3 than in EXP1, reflecting the changes in surface stress. Interestingly, the nearshore
383 region ($d \leq 80 \text{ km}$) has a higher TKE difference than the offshore region. This is likely
384 partly explained by the presence of the steady oceanic geostrophic jet that flows in the same
385 direction as the wind, reducing the surface stress near the coast.

386 Binned scatterplots of 1-month running means of wind curl and surface current vorticity
387 over the domain 30 °N - 45 °N and ($150 \text{ km} < d < 500 \text{ km}$) are calculated for EXP1 and
388 EXP3. EXP1, as expected, does not have any significant relationship between wind curl and
389 surface current vorticity (not shown). EXP3 has a clear linear relationship between them
390 (Fig. 10a). An non-dimensional coupling coefficient s_w is defined from the slope of the linear
391 regression estimated from the scatterplot. The positive s_w indicates a positive forcing of the
392 currents on the wind, a positive (negative) current vorticity inducing a positive (negative)
393 wind curl. The wind changes are explained by the surface stress changes, a weaker surface

394 stress allowing the wind to accelerate. s_w counteracts the effect expressed in s_{st} and hence
 395 acts to reduce s_{st} from EXP2 to EXP3. The positive s_w is also consistent with Fig. 5, the
 396 currents inducing a positive wind curl in the center of an anticyclonic eddy, that counteracts
 397 the current-induced negative surface stress curl. Fig. 10b depicts the vertical structure of
 398 the coupling coefficient s_w . The current feedback mainly shapes the surface wind, however,
 399 its effect can be felt up to 300m. Finally, a spectral analysis reveals the current feedback
 400 mainly affects the wind at eddy-scale (but can be slightly felt over several hundreds of km.),
 401 and over timescale between 30-days^{-1} and 300-days^{-1} (not shown). To our knowledge, this
 402 is an entirely new phenomenon that has not previously been pointed out. Finally, although
 403 the wind changes have an important effect on the oceanic response, from the atmospheric
 404 point of view, the changes are rather small. The Planetary Boundary Layer Height is not
 405 changed, nor the mean overlying circulation, the clouds or the precipitations. For more
 406 dynamical regions, we expect a larger large scale effect.

407 5. Induced Ekman Pumping and Eddy Attenuation Time

408 The current feedback to the atmosphere, by shaping the surface stress, induces an ad-
 409 ditional Ekman pumping in the ocean which provides a mechanism for weakening an eddy
 410 (*i.e.*, the eddy damping by the current feedback). The Ekman pumping is

$$w_{ek} = \mathbf{k} \cdot \nabla \times \frac{\boldsymbol{\tau}}{\rho_0 f}, \quad (12)$$

411 where f is the Coriolis frequency. Using the current coupling coefficient s_{st} from EXP3, (12)
 412 becomes

$$w_{ek} = \frac{s_{st} \Omega_{surf}}{\rho_0 f}. \quad (13)$$

413 where the surface current vorticity is $\Omega_{surf} = \mathbf{k}$. Using (12) and a typical $\Omega_{surf} = 1 \times 10^{-5} s^{-1}$
 414 on a scale of 100 km, $w_{ek} = 10 \text{ cm day}^{-1}$, which is similar to the estimate in Gaube et al.
 415 (2015).

416 An attenuation time scale of eddies is then estimated as a result of the current-induced
 417 surface stress curl and, to check the results from an energetic point of view, of sink of
 418 $F_e K_e$. In a similar way as described by Gaube et al. (2015), the decay time scale of an
 419 eddy associated with the stress curl can be estimated from a simplified vertically-integrated
 420 barotropic vorticity balance:

$$\frac{\partial \Omega_{bt}}{\partial t} = \mathbf{k} \cdot \nabla_c \times \frac{\boldsymbol{\tau}}{\rho_0}. \quad (14)$$

421 where the eddy barotropic vorticity is defined as the vorticity of the integrated velocities,

$$\Omega_{bt} = \frac{\partial \bar{v}^z}{\partial x} - \frac{\partial \bar{u}^z}{\partial y}. \quad (15)$$

422 $\nabla_c \times \boldsymbol{\tau}$ is the surface stress curl induced by the current feedback, and \bar{u}^z and \bar{v}^z are the zonal
 423 and meridional mean depth-averaged current component.

424 Figure 11 shows a snapshot of the surface current vorticity and a 2000 m vertically
 425 integrated current vorticity from EXP3. The integration is not to the bottom is to be able
 426 to neglect bottom drag effect on the eddies. At the surface there are small-scale features
 427 as filaments that are not present in the depth integral; however, the main eddies can be
 428 seen from both the surface vorticity and the depth-integrated vorticity, the depth-integrated
 429 vorticity being about 500 larger than the surface vorticity. Therefore, a characteristic vertical

430 scale of eddies $D = 500m$ can be estimated as a translation between the surface and depth-
 431 integrated vorticity:

$$\Omega_{bt} = D \Omega_{surf}, \quad (16)$$

432 Using (16) and the current coupling coefficient s_{st} , (14) becomes identical to Eq. (14) of
 433 Gaube et al. (2015):

$$\frac{\partial \Omega}{\partial t} = -\frac{f}{D} w_{ek}. \quad (17)$$

434 An eddy attenuation time scale can be estimated from (17) as

$$t_{vrt} = \frac{\rho_0 D}{s_{st}}. \quad (18)$$

435 As previously noted by Gaube *et al.*(2015), this estimate of eddy attenuation time depends
 436 only on D , and, in this study, the current coupling coefficient s_{st} and not on the eddy
 437 amplitude or radius. Note that s_{st} depends on the background wind that for the CCS is
 438 about $5ms^{-1}$. For an eddy with $D = 500m$ under a uniform background wind of $5ms^{-1}$ and
 439 using s_{st} from EXP2 ($s_{st} = 0.019N \ s \ m^{-3}$) or from EXP3 ($s_{st} = 0.012N \ s \ m^{-3}$), the eddy
 440 attenuation time is $t_{vrt} = 313$ days or $t_{vrt} = 495$ days, respectively. Not surprisingly, when
 441 neglecting the atmospheric adjustment, the eddy attenuation time scale is underestimated.
 442 Given (18) the shallower the mesoscale eddy is the shorter the eddy attenuation time.

443 This eddy attenuation time t_{vrt} can be directly compared to the one estimated from
 444 the observations by Gaube et al. (2015). From Eq. (19) in Gaube et al. (2015), the wind
 445 background here and a surface drag coefficient of $C_d = 0.012$ (Large and Pond 1981), the
 446 eddy attenuation time scale is 541 days, which is close to the t_{vrt} in EXP3, *i.e.*, by taking
 447 into account the atmospheric adjustment to the current feedback. An eddy attenuation time
 448 scale can also be estimated from an energy perspective, in that case, due to the quadratic

449 form of the EKE, such a timescale is equal to $t_{vrt}/2$ (roughly 250*days* for EXP3 and 156*days*
450 for EXP2).

451 In EXP3 the current feedback reduces the surface EKE by 44% (Fig. 1). However, it
452 only reduces the total integrated EKE by 27%. This is explained by the eddy attenuation
453 time scale that depends on the depth scale of the eddies and on the depth structure of the
454 eddy response. The shallower the eddies are, the more sensitive they are to the current
455 feedback. An alternative interpretation is that the wind damping at the surface changes the
456 vertical structure of the eddies over their lifetime (with the initial structure being set by the
457 baroclinic instability that generates them generally something close to the first baroclinic
458 mode). The anticyclonic eddy observed by (McGillicuddy et al. 2007) and the cyclonic
459 "thinny" described in a recent paper (McGillicuddy Jr 2015) may be examples of this.

460 6. Eddy Statistics

461 The eddy tracking method (Sec. 2f) was applied to EXP1, EXP3, and AVISO. Overall,
462 the simulations show a fair agreement with these observations and previous analyses (Chel-
463 ton et al. 2011; Kurian et al. 2011). Figure 12 shows the eddy sea-surface height (SSH)
464 amplitude and rotational speed distributions. The simulation EXP1 without current feed-
465 back overestimates the eddy SSH and rotational speed compared to the observations. It also
466 underestimates the eddy scale, and overestimates the eddy life (not shown), allowing the
467 eddies to propagate further offshore. This is consistent with the too-large offshore EKE in
468 EXP1 (Fig. 1). Due to a reduction of the eddy amplitude, rotational speed, and eddy life
469 (not shown), EXP3 presents a better agreement with the AVISO results through the eddy

470 killing mechanism.

471 Recently, Samelson et al. (2014) showed a composite life-cycle for a long-lived mesoscale
472 eddy: on average, the eddy first grows in SSH amplitude, then has a slow growth followed
473 by a slow symmetric decay, and, at the end, the eddy amplitude decreases rapidly before
474 collapsing (see for example Fig. 2 of Samelson et al. 2014). They show a stochastic model
475 was able to predict accurately the eddy life symmetry and thus suggest that the evolu-
476 tion of mesoscale structures is dominated by effectively stochastic interactions, rather than
477 by the classical wave mean cycle of initial growth followed by nonlinear equilibration and
478 barotropic, radiative, or frictional decay, or by the vortex merger processes of inverse tur-
479 bulent cascade theory. The lengthy stabilization of the composite eddy and its property
480 of symmetry between its growing and decay phases contradicts the results in Gaube et al.
481 (2015) and our own. The eddy should rapidly intensify as it forms, then eventually has a
482 slow growth, but then it should decay in an asymmetric way due the current feedback eddy
483 damping. Figure 13 shows the evolution of the normalized amplitude \mathcal{A} as a function of the
484 normalized time \mathcal{T} for all tracked eddies with a lifetime greater than 16 weeks (*cf.*, Fig. 2 in
485 Samelson et al. (2014)). As in Samelson et al. (2014), each eddy amplitude time series was
486 normalized by its time mean, and the respective lifetime (\mathcal{L}) by using the convention $\mathcal{T}1 = 0$
487 and $\mathcal{T}\mathcal{L} = 1$. In both EXP3 and AVISO, the eddy first grows in strength, then decreases
488 slowly (by 10%) from $\mathcal{T} = 0.3$ to $\mathcal{T} = 0.7$, and finally, decreases rapidly before collapsing
489 (presumably through some destructive interaction with other currents). This supports the
490 current induced eddy killing as a realistic mechanism. In EXP1 the systematic eddy decay
491 during its middle phase seems to be absent. The decay time scale of an eddy associated
492 with the current feedback is also estimated using Fig 13. During the slow decay present in

493 EXP3 (and not in EXP1), the eddy amplitude is reduced by 10% in roughly $0.4\mathcal{L}$. Using a
494 long-lived eddy mean life of 206 days, a decay time scale t_{eddy} of 527 days is estimated and
495 is consistent with the previous estimation of t_{vrt} and the Gaube et al. (2015) estimate. The
496 discrepancies with the (Samelson et al. 2014) results will need further investigation.

497 Figures 12-13 do show some discrepancies between EXP3 and AVISO. While no doubt
498 some of these are due to model bias, there are important sampling differences. In particular,
499 the AVISO data has spatial and temporal resolution issues, and sees only the larger mesoscale
500 eddies (Chelton et al. 2011).

501 7. Discussion and Conclusions

502 Using coupled ocean-atmosphere simulations, we assess the role of the current feedback
503 through the surface wind work, the energy transfer from the atmosphere to the ocean, and
504 its consequences for both oceanic and atmospheric mesoscale activity. In good agreement
505 with former studies we show the current feedback strongly attenuates the oceanic EKE. A
506 simplified EKE budget shows the current feedback acts on the eddy wind work $F_e K_e$ through
507 its geostrophic component. In the coastal region, it reduces the energy transfer from the
508 atmosphere to the ocean, while offshore it induces a deflection of the energy from the oceanic
509 geostrophic currents (eddies) to the atmosphere. As a results, there is less coastal generation
510 of EKE and damping or even killing of eddies offshore.

511 The current feedback can be split into two actions: (1) on the surface stress and (2) on the
512 wind. The action on the stress induces the EKE damping, by reducing the energy transfer
513 from the atmosphere to the ocean and even reversing it through the offshore geostrophic

514 currents. We determine for the U.S. West Coast the coupling coefficients between the oceanic
515 surface current and the surface stress, and between the oceanic surface current and the wind,
516 which are opposing effects. The current feedback has a negative action on the surface stress,
517 a positive (negative) surface vorticity inducing a negative (positive) stress curl. For the first
518 time, we show the wind response to the current feedback partly counteracts the stress effect
519 and therefore partly re-energizes the ocean. In the nearshore region, due to less transfer of
520 energy from the atmosphere to the ocean, the wind accelerates, increasing back the nearshore
521 surface stress and hence the coastal EKE generation. Offshore, there is a positive feedback:
522 a positive surface vorticity inducing a positive wind curl (leading to a positive coupling
523 coefficient), damping the negative current-induced surface stress curl. A simulation that
524 neglects the atmospheric adjustment to the reduced stress (as EXP2 or Eden and Dietze
525 (2009)), systematically overestimates the attenuation of the EKE. There is a route of energy
526 from the atmosphere into the nearshore ocean, offshore energy propagation in the ocean,
527 and then from the offshore ocean to the atmosphere.

528 Using the current-wind stress coupling coefficient, an eddy attenuation time scale is
529 estimated from a vorticity balance perspective. As shown previously by Gaube et al. (2015),
530 the derived eddy attenuation time scale scale depends on the characteristic vertical scale
531 of the eddies D and the current coupling coefficient s_{st} (which depends on the background
532 wind). Using mean parameters for the CCS, we estimate an eddy attenuation time scale of
533 $t_{vrt} = 495$ days which is consistent with the estimate in Gaube et al. (2015). A simulation
534 that neglects the atmospheric adjustment to the current feedback underestimates the eddy
535 attenuation time scale ($t_{vrt} = 313$ days in that case). We show a similar time scale can
536 be estimated during the slow decay period of the composite average life cycle of long-lived

537 eddies

538 Gaube et al. (2015) provides a satellite-based validation of our results. A more direct
539 validation is made here using eddy statistics applied on the coupled simulation without
540 current feedback (*i.e.*, EXP1) and on a fully coupled simulation (*i.e.*, EXP3). Consistent
541 with a reduction of the EKE, the coastal reduction of the energy transfer from the atmosphere
542 to the ocean and the sink of energy from the offshore ocean to the atmosphere actually reduce
543 the eddies amplitude and rotational speed in a realistic way. Simulations that resolve the
544 EKE and without current feedback (*i.e.*, forced by prescribed wind stress or a bulk formula
545 without current feedback) may systematically overestimate the EKE. We also show that the
546 current feedback to the atmosphere also reduces the eddy lifetime in EXP3 and is consistent
547 with the observed composite life-cycle of rapid early intensification, a prolonged middle stage
548 of slow decay due to eddy killing by the current feedback, and an abrupt collapse at the end.

549 A regional high-resolution atmospheric model is usually very costly compared to an
550 oceanic model. So an important next question is how best to force an uncoupled oceanic
551 model. A simulation that uses prescribed wind stress cannot damp the offshore eddies since
552 the prescribed wind stress is uncorrelated with the eddies. A bulk-forced oceanic simulation,
553 *i.e.*, where the model is forced by the wind, should estimate the surface stress using the rel-
554 ative wind. A distinction is necessary between observations or a fully coupled model, on the
555 one hand, and an uncoupled atmospheric wind product, on the other. For non-deterministic
556 variability (such as oceanic eddies), the bulk formulae used to estimate the surface stress
557 should in any case take into account a parameterization of the partial re-energization of the
558 ocean by the atmospheric response. The surface stress could be estimated with a velocity

559 that is the wind relative to the current corrected by the current-wind coupling coefficient s_w

$$\mathbf{U} = \mathbf{U}_a - (1 - s_w)\mathbf{U}_o, \quad (19)$$

560 For the U.S. West Coast, $s_w = 0.23$ can be derived from Fig. 10. However, it remains to
561 be seen how well this modified relative wind parameterization would work for an uncoupled
562 model, and the current-wind coupling coefficient found in this study may not be valid for
563 other regions, pending further investigation. The coupling coefficient depends on several
564 local parameters such as the background wind, the steadiness, and the EKE. Even for the
565 CCS, the wind coupling coefficient may not be accurate for the nearshore region; there the
566 wind adjustment is stronger, canceling more efficiently the reduction of energy transfer from
567 the atmosphere to the ocean. For deterministic features such an adjustment may not be
568 necessary if the model is forced by observations or some adequate representation of the
569 oceanic currents. For instance, for a U.S. West Coast configuration forced by the QuikSCAT
570 wind stress observations (*e.g.*, Capet et al. 2008a; Renault et al. 2015a), the simulated wind-
571 driven alongshore current perturbations may be correlated to the climatological average
572 currents and hence already contain both the atmospheric adjustment to the current feedback
573 and the reduction of the surface stress perturbations, allowing a good agreement of the EKE
574 close to the coast. However, the eddies generated are not correlated with the reality lying
575 behind the measured stress, so that such simulations can not represent the offshore sink
576 of energy from the ocean to the atmosphere, explaining their offshore EKE overestimation.
577 Finally, for low-resolution simulations (*e.g.*, Global Circulation Models), since the EKE is
578 already underestimated, taking into account the current feedback to the atmosphere would
579 induce a larger EKE underestimation, degrading the realism of the simulation.

580 The current effect on the wind speed should be assessed from the observations. A scat-
581 terometer (as QuikSCAT) is fundamentally a stress measuring instrument. The winds are
582 reported as so-called equivalent neutral stability winds, which is the wind that would exist
583 if the conditions were neutrally stable and the ocean current were zero. Therefore, it is not
584 possible to determine from scatterometry alone what the actual surface wind is. Dedicated
585 studies using scatterometer and other observations (*e.g.*, *in situ* ones) should aim to address
586 this issue.

587 In this study of the CCS, although the perturbations are clearly modulated by the current
588 feedback, the mean surface stress and current are not significantly changed. However, they
589 may be impacted in other regions with stronger currents and or stronger SST fronts, such as
590 the Gulf Stream area. An expanded Lorenz diagram of the depth-integrated energy budget
591 (Lorenz 1955) for the ocean could include a sink of energy by negative geostrophic wind work
592 induced by the current feedback. Consistent with Wang and Huang (2004), the total $F_e K_e$ is
593 much larger than its geostrophic component $F_e K_{eg}$. Substantial power goes into the surface
594 Ekman currents, (Wang and Huang 2004), and much of this is dissipated within the upper
595 few tens of meter (*i.e.*, in the Ekman layer) and therefore is not available to drive currents
596 and diapycnal mixing deeper in the water column. Two strong pathways of mechanical
597 energy from the surface to the deeper ocean are clear at present: wind forcing of near-
598 inertial oscillations and wind forcing of surface Ekman currents and geostrophic flow (Alford
599 2003, Watanabe and Hibiya 2002, Scott and Xu 2009)). In EXP3, $F_e K_e$ integrated over the
600 whole domain is an energy conversion of $16.9 \times 10^6 m^5 s^{-3}$, whereas $F_e K_{eg}$ is only 2.1×10^6
601 $m^5 s^{-3}$. We show the current feedback to the atmosphere mainly acts through the latter.
602 Figure 14 expands the Lorenz diagram of energy conversion for the depth-integrated EKE,

603 integrated over the whole U.S. West Coast domain during the 1995-1999 period. It includes
 604 the geostrophic wind work $F_e K_{eg}$, and the baroclinic ($P_e K_e$) and barotropic conversions
 605 ($K_m K_e$). Several energy conversion arrows are added: the current induced eddy geostrophic
 606 wind work, $F_e K_{egc} = F_e K_{eg_EXP1} - F_e K_{eg_EXP3}$, the current-induced baroclinic conversion,
 607 $P_e K_{ec} = P_e K_{e_EXP1} - P_e K_{e_EXP3}$, and the current-induced barotropic conversion $K_m K_{ec} =$
 608 $K_m K_{e_EXP1} - K_m K_{e_EXP3}$. $F_e K_{egc}$ represents 29% of the total energy input (defined as
 609 the sum of $F_e K_{eg}$, $P_e K_e$, and $K_m K_e$), and 43% of $F_e K_{eg}$. The baroclinic and barotropic
 610 conversions adjust to slightly counteract the wind work reduction, inducing a positive power
 611 input of 3% of the total eddy energy input. The EKE input is then reduced by 26%, that
 612 roughly corresponds to the depth-integrated EKE reduction (27%).

613 In summary, ocean-atmosphere models should take into account the current feedback
 614 to have a realistic representation of the EKE and its associated processes. This might be
 615 even more important for biogeochemical models. In the open ocean, and in particular in
 616 low-nutrient environments, mesoscale processes increase the net upward flux of limiting nu-
 617 trients and enhance biological production (Martin and Richards 2001; McGillicuddy et al.
 618 2007; Gaube et al. 2013). McGillicuddy et al. (2007), using observations, show the effects of
 619 surface currents on Ekman pumping in eddies and, in particular how it affects the biology.
 620 In the EBUS, the eddies modulate biological productivity by subducting nutrients out of
 621 the euphotic zone and advecting biogeochemical material offshore (Gruber et al. 2011; Nagai
 622 et al. 2015; Renault et al. 2015a). A simulation without current feedback, by overestimat-
 623 ing the eddy amplitude, lifetime, and spatial range, may overestimate their quenching and
 624 offshore transport effects on the biogeochemical materials. We intend to investigate this
 625 soon.

626 *Acknowledgments.*

627 We appreciate support from the Office of Naval Research (ONR N00014-12-1-0939),
628 the National Science Foundation (OCE-1419450), the NASA grants NNX13AD78G and
629 NNX14AM72G, the California Ocean Protection Council grant, and the Bureau of Ocean
630 Energy Management. This work used the Extreme Science and Engineering Discovery En-
631 vironment (XSEDE) and Yellowstone (NCAR). The authors want to thank two anonymous
632 reviewers and Peter Gaube for their comments, as well as Sebastien Masson and Roger
633 Samelson for useful discussions

634

635 REFERENCES

- 636 Alford, M. H., 2003: Improved global maps and 54-year history of wind-work on ocean
637 inertial motions. *Geophysical Research Letters*, **30** (8).
- 638 Beckmann, A. and D. B. Haidvogel, 1993: Numerical simulation of flow around a tall iso-
639 lated seamount. part i: Problem formulation and model accuracy. *Journal of Physical*
640 *Oceanography*, **23** (8), 1736–1753.
- 641 Capet, X., F. Colas, P. Penven, P. Marchesiello, and J. C. McWilliams, 2008a: Ed-
642 dies in eastern-boundary subtropical upwelling systems. *Ocean Modeling in an Eddy-*
643 *ing Regime*, *Geophys. Monogr. Ser.*, M. Hecht and H. Hasumi, Eds., AGU, 131–147,
644 doi:10.1029/177GM10.

- 645 Capet, X., P. Marchesiello, and J. McWilliams, 2004: Upwelling response to coastal wind
646 profiles. *Geophysical Research Letters*, **31** (13).
- 647 Capet, X., J. McWilliams, M. Molemaker, and A. Shchepetkin, 2008b: Mesoscale to subme-
648 soscale transition in the California Current System. part i: Flow structure, eddy flux, and
649 observational tests. *Journal of Physical Oceanography*, **38** (1), 29–43.
- 650 Carr, M.-E. and E. J. Kearns, 2003: Production regimes in four Eastern Boundary Current
651 Systems. *Deep Sea Research Part II: Topical Studies in Oceanography*, **50** (22), 3199–3221.
- 652 Carton, J. A. and B. S. Giese, 2008: A reanalysis of ocean climate using simple ocean data
653 assimilation (soda). *Monthly Weather Review*, **136** (8), 2999–3017.
- 654 Chaigneau, A., M. Le Texier, G. Eldin, C. Grados, and O. Pizarro, 2011: Vertical structure
655 of mesoscale eddies in the eastern south pacific ocean: A composite analysis from altimetry
656 and argo profiling floats. *Journal of Geophysical Research: Oceans*, **116** (C11).
- 657 Chelton, D. B., M. G. Schlax, M. H. Freilich, and R. F. Milliff, 2004: Satellite measurements
658 reveal persistent small-scale features in ocean winds. *science*, **303** (5660), 978–983.
- 659 Chelton, D. B., M. G. Schlax, and R. M. Samelson, 2007: Summertime coupling between sea
660 surface temperature and wind stress in the California Current System. *Journal of Physical
661 Oceanography*, **37** (3), 495–517.
- 662 Chelton, D. B., M. G. Schlax, and R. M. Samelson, 2011: Global observations of nonlinear
663 mesoscale eddies. *Progress in Oceanography*, **91** (2), 167–216.

664 Chou, M.-D. and M. J. Suarez, 1999: A solar radiation parameterization for atmospheric
665 studies. *NASA Tech. Memo*, **104606**, 40.

666 Colas, F., X. Capet, J. C. McWilliams, and Z. Li, 2013: Mesoscale eddy buoyancy flux and
667 eddy-induced circulation in Eastern Boundary Currents. *Journal of Physical Oceanogra-*
668 *phy*, **43 (6)**, 1073–1095.

669 Cornillon, P. and K. Park, 2001: Warm core ring velocities inferred from nscat. *Geophysical*
670 *research letters*, **28 (4)**, 575–578.

671 Dawe, J. T. and L. Thompson, 2006: Effect of ocean surface currents on wind stress, heat
672 flux, and wind power input to the ocean. *Geophysical research letters*, **33 (9)**.

673 Debreu, L., P. Marchesiello, P. Penven, and G. Cambon, 2012: Two-way nesting in split-
674 explicit ocean models: algorithms, implementation and validation. *Ocean Modelling*, **49**,
675 1–21.

676 Dewar, W. K. and G. R. Flierl, 1987: Some effects of the wind on rings. *Journal of physical*
677 *oceanography*, **17 (10)**, 1653–1667.

678 Ducet, N., P.-Y. Le Traon, and G. Reverdin, 2000: Global high-resolution mapping of ocean
679 circulation from topex/poseidon and ers-1 and-2. *Journal of Geophysical Research-Oceans*,
680 **105 (C8)**, 19 477–19 498.

681 Duhaut, T. H. and D. N. Straub, 2006: Wind stress dependence on ocean surface veloc-
682 ity: Implications for mechanical energy input to ocean circulation. *Journal of physical*
683 *oceanography*, **36 (2)**, 202–211.

684 Eden, C. and H. Dietze, 2009: Effects of mesoscale eddy/wind interactions on biological
685 new production and eddy kinetic energy. *Journal of Geophysical Research: Oceans (1978–*
686 *2012)*, **114 (C5)**.

687 Edwards, K. A., A. M. Rogerson, C. D. Winant, and D. P. Rogers, 2001: Adjustment of the
688 marine atmospheric boundary layer to a coastal cape. *Journal of the atmospheric sciences*,
689 **58 (12)**, 1511–1528.

690 FAO, 2009: State of the World’s Fisheries and Aquaculture 2008. *Food and Agriculture*
691 *Organization of the United Nations*.

692 Gaube, P., D. B. Chelton, R. M. Samelson, M. G. Schlax, and L. W. O'Neill, 2015: Satellite
693 observations of mesoscale eddy-induced ekman pumping. *Journal of Physical Oceanogra-*
694 *phy*, **45 (1)**, 104–132.

695 Gaube, P., D. B. Chelton, P. G. Strutton, and M. J. Behrenfeld, 2013: Satellite observations
696 of chlorophyll, phytoplankton biomass, and ekman pumping in nonlinear mesoscale eddies.
697 *Journal of Geophysical Research: Oceans*, **118 (12)**, 6349–6370.

698 Gruber, N., Z. Lachkar, H. Frenzel, P. Marchesiello, M. Münnich, J. C. McWilliams, T. Na-
699 gai, and G.-K. Plattner, 2011: Eddy-induced reduction of biological production in Eastern
700 Boundary Upwelling Systems. *Nature geoscience*, **4 (11)**, 787–792.

701 Hong, S.-Y. and J.-O. J. Lim, 2006: The wrf single-moment 6-class microphysics scheme
702 (wsm6). *J. Korean Meteor. Soc.*, **42 (2)**, 129–151.

703 Hong, S.-Y., Y. Noh, and J. Dudhia, 2006: A new vertical diffusion package with an explicit
704 treatment of entrainment processes. *Monthly Weather Review*, **134 (9)**, 2318–2341.

705 Hughes, C. W. and C. Wilson, 2008: Wind work on the geostrophic ocean circulation: An
706 observational study of the effect of small scales in the wind stress. *Journal of Geophysical*
707 *Research: Oceans (1978–2012)*, **113 (C2)**.

708 Jin, X., C. Dong, J. Kurian, J. C. McWilliams, D. B. Chelton, and Z. Li, 2009: Sst-wind
709 interaction in coastal upwelling: Oceanic simulation with empirical coupling. *Journal of*
710 *Physical Oceanography*, **39 (11)**, 2957–2970.

711 Jousse, A., L. Renault, and A. Hall, 2015: Climatic importance of aerosol indirect effects in
712 the northeast pacific. *Submitted to Journal of Climate*.

713 Kurian, J., F. Colas, X. Capet, J. C. McWilliams, and D. B. Chelton, 2011: Eddy properties
714 in the california current system. *Journal of Geophysical Research: Oceans (1978–2012)*,
715 **116 (C8)**.

716 Large, W. and S. Pond, 1981: Open ocean momentum flux measurements in moderate to
717 strong winds. *Journal of physical oceanography*, **11 (3)**, 324–336.

718 Large, W. B., 2006: Surface fluxes for practitioners of global ocean data assimilation. *Ocean*
719 *Weather Forecasting*, Springer, 229–270.

720 Large, W. G., J. C. McWilliams, S. C. Doney, et al., 1994: Oceanic vertical mixing: A review
721 and a model with a nonlocal boundary layer parameterization. *Reviews of Geophysics*,
722 **32 (4)**, 363–404.

723 Lathuilière, C., V. Echevin, M. Lévy, and G. Madec, 2010: On the role of the mesoscale
724 circulation on an idealized coastal upwelling ecosystem. *Journal of Geophysical Research:*
725 *Oceans (1978–2012)*, **115 (C9)**.

- 726 Lemarié, F., 2015: Numerical modification of atmospheric models to include the feedback of
727 oceanic currents on air-sea fluxes in ocean-atmosphere coupled models. Technical Report
728 RT-464, INRIA Grenoble - Rhône-Alpes ; Laboratoire Jean Kuntzmann ; Université de
729 Grenoble I - Joseph Fourier ; INRIA. URL <https://hal.inria.fr/hal-01184711>.
- 730 Lorenz, E. N., 1955: Available potential energy and the maintenance of the general circula-
731 tion. *Tellus*, **7** (2), 157–167.
- 732 Marchesiello, P., J. C. McWilliams, and A. Shchepetkin, 2001: Open boundary conditions
733 for long-term integration of regional oceanic models. *Ocean modelling*, **3** (1), 1–20.
- 734 Marchesiello, P., J. C. McWilliams, and A. Shchepetkin, 2003: Equilibrium structure and
735 dynamics of the California Current System. *Journal of Physical Oceanography*, **33** (4),
736 753–783.
- 737 Martin, A. P. and K. J. Richards, 2001: Mechanisms for vertical nutrient transport within a
738 north atlantic mesoscale eddy. *Deep Sea Research Part II: Topical Studies in Oceanography*,
739 **48** (4), 757–773.
- 740 Mason, E., J. Molemaker, A. F. Shchepetkin, F. Colas, J. C. McWilliams, and P. Sangrà,
741 2010: Procedures for offline grid nesting in regional ocean models. *Ocean Modelling*,
742 **35** (1), 1–15.
- 743 McGillicuddy, D. J., et al., 2007: Eddy/wind interactions stimulate extraordinary mid-ocean
744 plankton blooms. *Science*, **316** (5827), 1021–1026.
- 745 McGillicuddy Jr, D. J., 2015: Formation of intrathermocline lenses by eddy–wind interaction.
746 *Journal of Physical Oceanography*, **45** (2), 606–612.

747 Minobe, S., A. Kuwano-Yoshida, N. Komori, S.-P. Xie, and R. J. Small, 2008: Influence of
748 the gulf stream on the troposphere. *Nature*, **452 (7184)**, 206–209.

749 Nagai, T., N. Gruber, H. Frenzel, Z. Lachkar, J. C. McWilliams, and G.-K. Plattner, 2015:
750 Dominant role of eddies and filaments in the offshore transport of carbon and nutrients in
751 the california current system. *Journal of Geophysical Research: Oceans*.

752 Nakanishi, M. and H. Niino, 2006: An improved mellor–yamada level-3 model: Its numer-
753 ical stability and application to a regional prediction of advection fog. *Boundary-Layer*
754 *Meteorology*, **119 (2)**, 397–407.

755 Park, H., D. Lee, W.-P. Jeon, S. Hahn, J. Kim, J. Kim, J. Choi, and H. Choi, 2006: Drag
756 reduction in flow over a two-dimensional bluff body with a blunt trailing edge using a new
757 passive device. *Journal of Fluid Mechanics*, **563**, 389–414.

758 Park, S. and C. S. Bretherton, 2009: The University of Washington shallow convection and
759 moist turbulence schemes and their impact on climate simulations with the community
760 atmosphere model. *Journal of Climate*, **22 (12)**, 3449–3469.

761 Perlin, N., E. D. Skyllingstad, and R. M. Samelson, 2011: Coastal atmospheric circulation
762 around an idealized cape during wind-driven upwelling studied from a coupled ocean-
763 atmosphere model. *Monthly Weather Review*, **139 (3)**, 809–829.

764 Perlin, N., E. D. Skyllingstad, R. M. Samelson, and P. L. Barbour, 2007: Numerical sim-
765 ulation of air-sea coupling during coastal upwelling. *Journal of Physical Oceanography*,
766 **37 (8)**, 2081–2093.

767 Renault, L., C. Deutsch, J. McWilliams, H. Frenzel, J. Liang, and F. Colas, 2015a: Coastal
768 wind pattern modulates biological productivity in california upwelling. *Submitted to Nature*
769 *Geoscience*.

770 Renault, L., B. Dewitte, M. Falvey, R. Garreaud, V. Echevin, and F. Bonjean, 2009: Impact
771 of atmospheric coastal jet off central Chile on sea surface temperature from satellite obser-
772 vations (2000–2007). *Journal of Geophysical Research: Oceans (1978–2012)*, **114 (C8)**.

773 Renault, L., A. Hall, and J. C. McWilliams, 2015b: Orographic shaping of u.s. west coast
774 wind profiles during the upwelling season. *Climate Dynamics*, 1–17.

775 Renault, L., et al., 2012: Upwelling response to atmospheric coastal jets off central Chile:
776 A modeling study of the October 2000 event. *Journal of Geophysical Research: Oceans*
777 *(1978–2012)*, **117 (C2)**.

778 Saha, S., et al., 2010: The NCEP climate forecast system reanalysis. *Bulletin of the American*
779 *Meteorological Society*, **91 (8)**, 1015–1057.

780 Samelson, R., M. Schlax, and D. Chelton, 2014: Randomness, symmetry, and scaling of
781 mesoscale eddy life cycles. *Journal of Physical Oceanography*, **44 (3)**, 1012–1029.

782 Sandwell, D. T. and W. H. Smith, 1997: Marine gravity anomaly from Geosat and ERS 1
783 satellite altimetry. *Journal of Geophysical Research: Solid Earth (1978–2012)*, **102 (B5)**,
784 10 039–10 054.

785 Scott, R. B. and Y. Xu, 2009: An update on the wind power input to the surface geostrophic
786 flow of the world ocean. *Deep Sea Research Part I: Oceanographic Research Papers*, **56 (3)**,
787 295–304.

788 Seo, H., A. J. Miller, and J. R. Norris, 2015: Eddy-wind interaction in the california current
789 system: dynamics and impacts. *Journal of Physical Oceanography*, **(2015)**.

790 Shchepetkin, A. F. and J. C. McWilliams, 2005: The regional oceanic modeling sys-
791 tem (roms): a split-explicit, free-surface, topography-following-coordinate oceanic model.
792 *Ocean Modelling*, **9 (4)**, 347–404.

793 Shchepetkin, A. F. and J. C. McWilliams, 2009: Correction and commentary for ocean fore-
794 casting in terrain-following coordinates: Formulation and skill assessment of the regional
795 ocean modeling system by haidvogel et al., j. comp. phys. 227, pp. 3595–3624. *Journal of*
796 *Computational Physics*, **228 (24)**, 8985–9000.

797 Skamarock, W., J. Klemp, J. Dudhia, D. Gill, and D. Barker, 2008: Coauthors, 2008: A
798 description of the Advanced Research wrf version 3. ncar tech. Tech. rep., Note NCAR/TN-
799 4751STR.

800 Spall, M. A., 2007: Midlatitude wind stress-sea surface temperature coupling in the vicinity
801 of oceanic fronts. *Journal of climate*, **20 (15)**, 3785–3801.

802 Wang, W. and R. X. Huang, 2004: Wind energy input to the ekman layer*. *Journal of*
803 *Physical Oceanography*, **34 (5)**, 1267–1275.

804 Watanabe, M. and T. Hibiya, 2002: Global estimates of the wind-induced energy flux to
805 inertial motions in the surface mixed layer. *Geophysical research letters*, **29 (8)**, 64–1.

806 Zhang, C., Y. Wang, and K. Hamilton, 2011: Improved representation of boundary layer
807 clouds over the southeast pacific in arw-wrf using a modified tiedtke cumulus parameter-
808 ization scheme. *Monthly Weather Review*, **139 (11)**, 3489–3513.

809 **List of Tables**

810 1 Sensitivity Experiments

41

TABLE 1. Sensitivity Experiments

Experiments	Current feedback
EXP1	None
EXP2	Only in surface stress, using atmosphere from EXP1
EXP3	In both surface stress and on atmosphere

811 List of Figures

- 812 1 Top panel: Mean surface Eddy Kinetic Energy (EKE, cm^2s^{-2}) from EXP1,
813 EXP2, and EXP3. Bottom panel: Temporal evolution of the EKE averaged
814 over the whole domain. The difference percentages between the uncoupled
815 experiments and the coupled experiment are indicated. There is a reduction
816 of the EKE when using the current to estimate the surface stress. The atmo-
817 spheric response damps the EKE reduction. From EXP1 to EXP2, the EKE
818 is reduced by 55%, whereas from EXP1 to EXP3, the EKE is reduced by 40%. 49
- 819 2 Depth-integrated EKE-budget components (cm^3s^{-3}) from EXP1 (top) and
820 EXP3 (bottom): from left to right: the eddy wind work (F_eK_e), the baroclinic
821 conversion (P_eK_e), and the barotropic conversion (K_mK_e). F_eK_e and P_eK_e
822 are the main energy source terms. The reduction of the EKE in Fig. 1 is
823 explained by the reduction of F_eK_e by the current feedback. 50

824 3 a) $F_e K_e$ cross-shore profiles ($cm^3 s^{-3}$) averaged between $30^\circ N$ and $45^\circ N$ from
825 EXP1 (blue), EXP2 (black), and EXP3 (red), (b) Differences between EXP1
826 and EXP2 (black), and EXP1 and EXP3 (red). c) same than (a) but for
827 $F_e K_{eg}$, (d) same than (b) but for the geostrophic eddy wind work $F_e K_{eg}$. The
828 total differences over the box [$30^\circ N$ and $45^\circ N$ x $d=500$ km] between EXP1
829 and the other experiments are indicated in the legend inlet. Two regions can
830 be distinguished: the coastal region (cross-shore distance $d < 80$ km), and
831 the offshore region ($d > 80$ km). In the coastal region, there is a reduction of
832 $F_e K_e$ mainly through its geostrophic component, in the offshore region, there
833 is an actual sink of $F_e K_e$ again through its geostrophic component ($F_e K_{eg}$).
834 The wind response to the current damps the $F_e K_e$ reduction. 51

835 4 Geostrophic eddy wind work ($F_e K_{eg}$) from EXP1 and EXP3. The reduction
836 of $F_e K_e$ is mainly explained by a coastal reduction of $F_e K_{eg}$, and an offshore
837 sink of energy through $F_e K_{eg}$. 52

838 5 Schematic representation of the current feedback effects over an anticyclonic
 839 eddy, considering a uniform southward wind. The green, black, and blue ar-
 840 rows represent the wind, surface stress, and surface current, respectively. The
 841 red (blue) shade indicates a positive (negative) $F_e K_e$. The black (green) +/-
 842 signs indicate the current-induced stress (wind) curl. a) A simulation with-
 843 out current feedback (*e.g.*, EXP1), b) A simulation that takes into account
 844 the current feedback into the estimation of the surface stress but neglects the
 845 atmospheric response (*e.g.*, EXP2), and c) A fully coupled simulation, *i.e.*,
 846 , that has the current feedback into the surface stress estimate and the at-
 847 mospheric response (*e.g.*, EXP3). In EXP1 (*i.e.*, simulations without current
 848 feedback), the net $F_e K_e$ is equal to zero. In EXP2 (*i.e.*, simulations with
 849 current feedback to the surface stress), over an eddy, the amount of positive
 850 wind work ($F_e K_e$) is reduced and the amount of negative $F_e K_e$ becomes more
 851 negative. As a result, the net $F_e K_e$ becomes negative, deflecting energy out
 852 of the eddy to the atmosphere. In a fully coupled model (EXP3), the atmo-
 853 spheric response damps the sink of $F_e K_e$ by increasing the positive $F_e K_e$ and
 854 decreasing the negative $F_e K_e$, the net $F_e K_e$ remaining negative. The current
 855 feedback induces a positive (negative) stress curl (wind curl) in the eddy's
 856 center.

53

857 6 Schematic representation of the current feedback considering a uniform south-
858 ward wind blowing along the coast. a) A simulation without current feedback
859 (*e.g.*, EXP1), b) A simulation that takes into account the current feedback
860 into the estimation of the surface stress but neglects the atmospheric response
861 (*e.g.*, EXP2), and c) A fully coupled simulation, *i.e.*, that has the current feed-
862 back into the stress estimate and the atmospheric response (*e.g.*, EXP3). The
863 green, black, and blue arrows represent the wind, surface stress, and oceanic
864 surface current, respectively. The red shade represents the induced $F_e K_e$ (pos-
865 itive in all cases). The wind induces an oceanic coastal geostrophic jet that
866 is partially in the same as direction than the wind, inducing a positive $F_e K_e$.
867 From EXP1 to EXP2, the reduction of the stress induces in turn a weakening
868 of $F_e K_e$. From EXP2 to EXP3, the wind accelerates, increasing back toward
869 its initial value the surface stress and hence $F_e K_e$ and the oceanic coastal
870 geostrophic jet. 54

871 7 a) Temporal 1D co-spectrum of the total wind work FK from EXP1 and EXP3
872 between 30°N and 45°N for the offshore region ($d > 80\text{ km}$), b) Difference
873 between EXP1 and EXP3. c) Same than (a) but for the geostrophic wind
874 work, d) same as b) for the geostrophic wind work. The current feedback to
875 the atmosphere act as an eddy killer by reducing $F_e K_e$ through its geostrophic
876 component, deflecting energy from the ocean to the atmosphere. 55

877 8 Binned scatterplot of the full time series of 1-month running means of surface
878 stress curl and surface current vorticity over the domain $30^\circ\text{N} - 45^\circ\text{N}$ and
879 $(150\text{ km} < d < 500\text{ km})$. The bars indicate plus and minus one the standard
880 deviation about the average drawn by stars. The linear regression is indicated
881 by a black line and the slope s_{st} is indicated in the title ($10^{-2} N s m^{-3}$). From
882 the left to the right: EXP1, EXP2, and EXP3. EXP1 does not have a signif-
883 icant slope since it does not have the current feedback to the atmosphere nor
884 the surface stress. EXP2 and EXP3 presents a clear negative linear relation-
885 ship between the currents and the stress curl. The currents feedback induce
886 fine scale wind stress structure. Consistently with the previous results, the
887 atmospheric response reduces the current feedback effect on the stress. 56

888 9 a) Cross-shore profile of the Turbulent Kinetic Energy (TKE) of the surface
889 wind averaged between 30°N and 45°N from EXP1 (cyan) and EXP3 (red).
890 The $F_e K_e$ sink from the ocean to the atmosphere results in a slightly larger
891 TKE in EXP3 compared to EXP1. In the nearshore region, there is a larger
892 wind enhancement that is likely partly explained by the presence of the steady
893 oceanic geostrophic jet that flows in the same direction as the wind. 57

- 894 10 a) Same as Fig. 8 but for the wind curl and the surface current vorticity for
895 EXP3. There is a positive linear relationship between the current vorticity
896 and the wind curl, *i.e.*, the current feedback on the atmosphere induces fine
897 scale structures in the wind field that counteract the current-induced stress
898 structure (Fig. 8). This explains the damping of the current feedback effect
899 on the EKE (see text). The linear regression is indicated by a black line and
900 the dimensionless slope s_w is indicated in the title. b) Vertical attenuation of
901 s_w with respect to the surface s_w . 58
- 902 11 a) Snapshot of sea surface relative vorticity and b) 2000 m integrated relative
903 vorticity, from EXP3. The colorbar scale is adjusted between (a) and (b) by a
904 factor of $D = 500$ that allows to have a rough match between the two panels.
905 D factor is interpreted as the characteristic vertical scale of the eddies. 59
- 906 12 Long-lived (16 weeks) eddy amplitude and rotational speed statistics from
907 EXP1 (blue), EXP3 (red), and AVISO (green). Consistently with the previous
908 results, the current feedback to the atmosphere damps the eddy amplitude and
909 rotational speed, improving the realism of the simulation. 60
- 910 13 Evolution of eddy normalized amplitude \mathcal{A} as a function of their dimensionless
911 time \mathcal{T} for all tracked eddies with a lifetime greater than 16 weeks. The blue,
912 red, and green colors represent the results from EXP1, EXP3, and AVISO. In
913 EXP3, consistently with AVISO, the eddy first grows in size, then, due to the
914 current feedback to the atmosphere, decreases slowly, and finally, decreases
915 rapidly before collapsing. In EXP1, the slow decrease is not evident. 61

916 14 An expanded Lorenz diagram of energy conversion for the depth-integrated
917 EKE, integrated over the whole U.S. West Coast domain for the period 1995-
918 1999. The atmosphere is above and mean ocean KE and PE to the left (not
919 represented). The current feedback to the atmosphere mainly removes energy
920 from the ocean to the atmosphere through the geostrophic flow. The mean
921 integrated values for each conversion term are indicated in $m^5 s^{-3}$. ϵ is the
922 dissipation term, and BF the energy flux o through the boundary. See text
923 for more information.

62

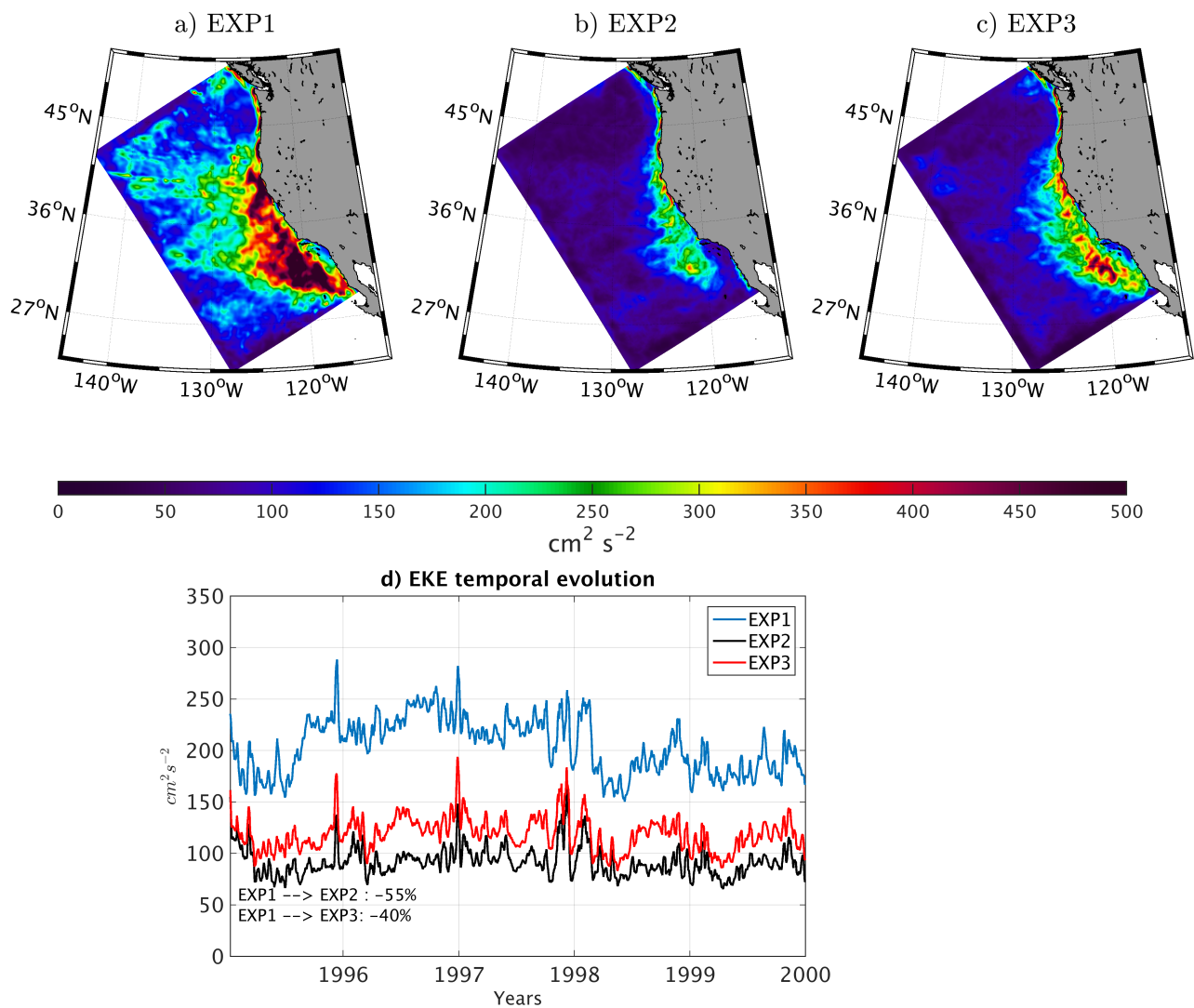


FIG. 1. Top panel: Mean surface Eddy Kinetic Energy (EKE, $cm^2 s^{-2}$) from EXP1, EXP2, and EXP3. Bottom panel: Temporal evolution of the EKE averaged over the whole domain. The difference percentages between the uncoupled experiments and the coupled experiment are indicated. There is a reduction of the EKE when using the current to estimate the surface stress. The atmospheric response damps the EKE reduction. From EXP1 to EXP2, the EKE is reduced by 55%, whereas from EXP1 to EXP3, the EKE is reduced by 40%.

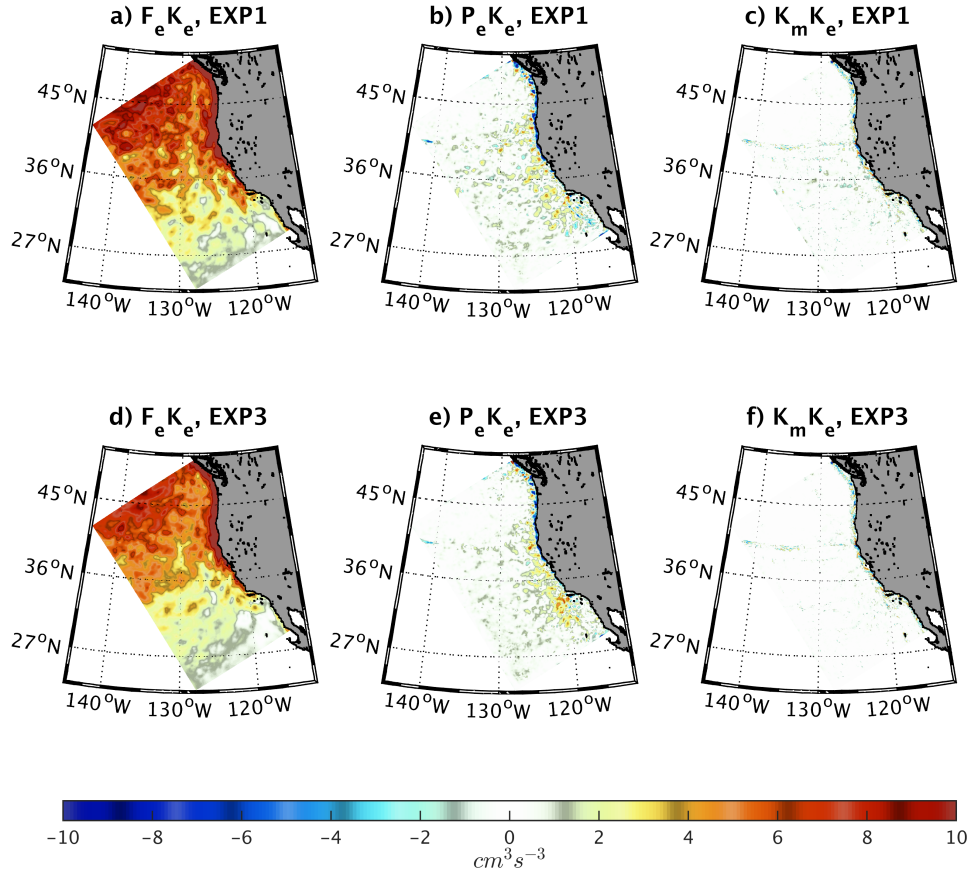


FIG. 2. Depth-integrated EKE-budget components ($cm^3 s^{-3}$) from EXP1 (top) and EXP3 (bottom): from left to right: the eddy wind work ($F_e K_e$), the baroclinic conversion ($P_e K_e$), and the barotropic conversion ($K_m K_e$). $F_e K_e$ and $P_e K_e$ are the main energy source terms. The reduction of the EKE in Fig. 1 is explained by the reduction of $F_e K_e$ by the current feedback.

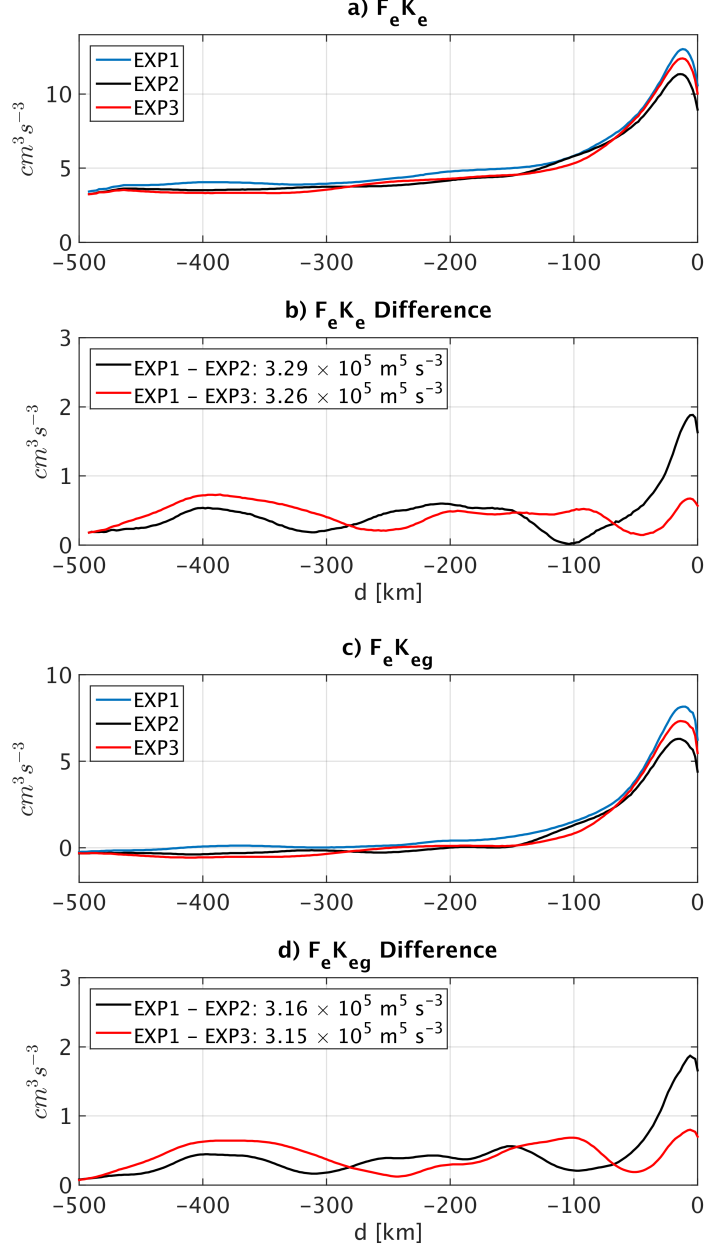


FIG. 3. a) $F_e K_e$ cross-shore profiles ($cm^3 s^{-3}$) averaged between $30^\circ N$ and $45^\circ N$ from EXP1 (blue), EXP2 (black), and EXP3 (red), (b) Differences between EXP1 and EXP2 (black), and EXP1 and EXP3 (red). c) same than (a) but for $F_e K_{eg}$, (d) same than (b) but for the geostrophic eddy wind work $F_e K_{eg}$. The total differences over the box [$30^\circ N$ and $45^\circ N$ x $d=500$ km] between EXP1 and the other experiments are indicated in the legend inlet. Two regions can be distinguished: the coastal region (cross-shore distance $d < 80$ km), and the offshore region ($d > 80$ km). In the coastal region, there is a reduction of $F_e K_e$ mainly through its geostrophic component, in the offshore region, there is an actual sink of $F_e K_e$ again through its geostrophic component ($F_e K_{eg}$). The wind response to the current damps the $F_e K_e$ reduction.

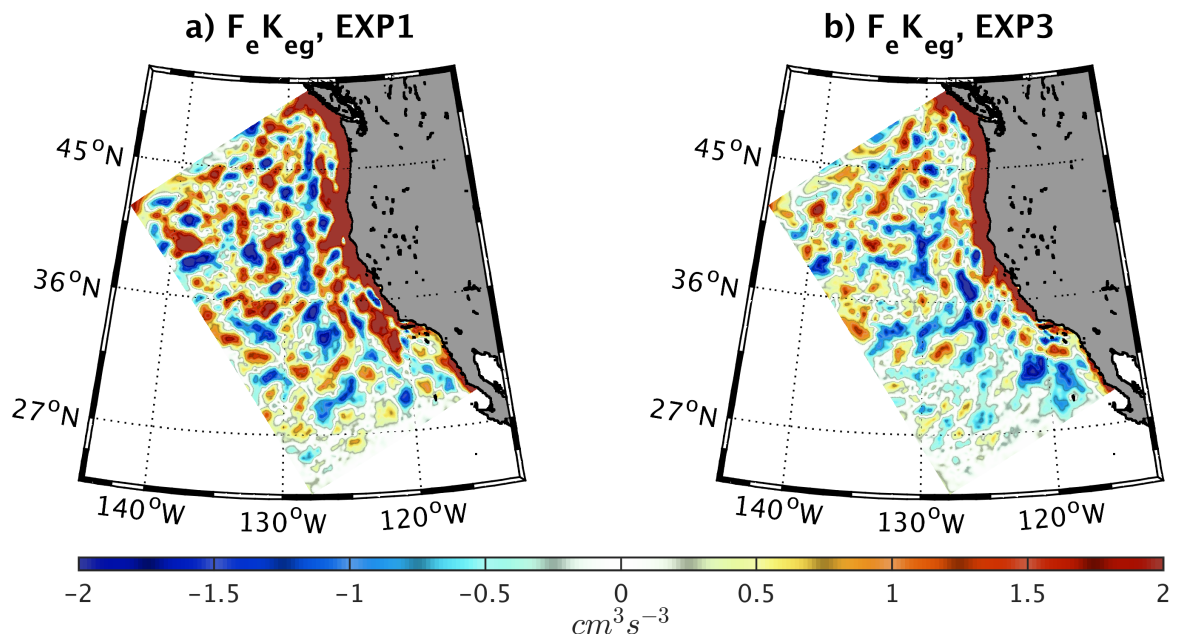


FIG. 4. Geostrophic eddy wind work ($F_e K_{eg}$) from EXP1 and EXP3. The reduction of $F_e K_e$ is mainly explained by a coastal reduction of $F_e K_{eg}$, and an offshore sink of energy through $F_e K_{eg}$.

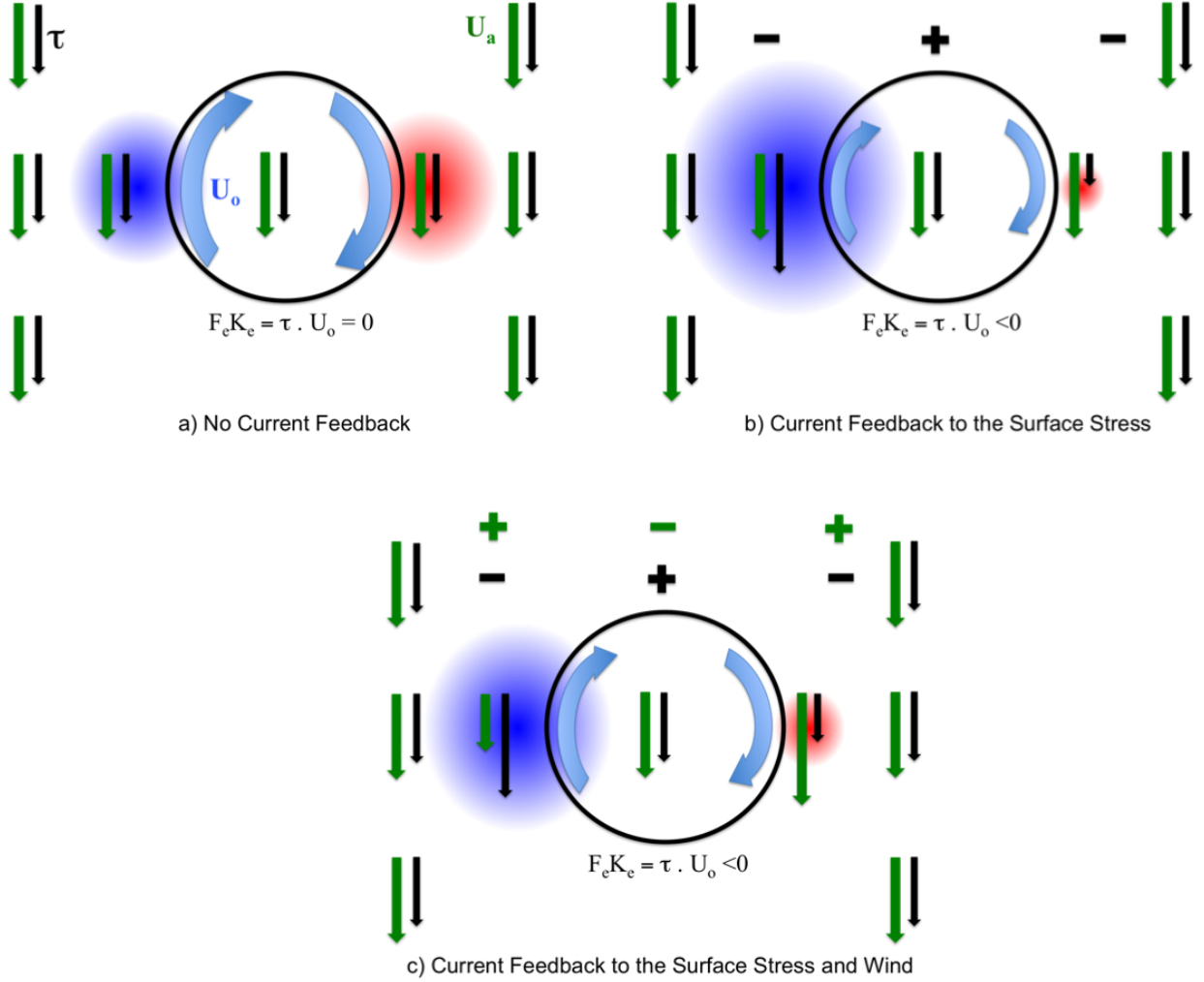


FIG. 5. Schematic representation of the current feedback effects over an anticyclonic eddy, considering a uniform southward wind. The green, black, and blue arrows represent the wind, surface stress, and surface current, respectively. The red (blue) shade indicates a positive (negative) $F_e K_e$. The black (green) +/- signs indicate the current-induced stress (wind) curl. a) A simulation without current feedback (*e.g.*, EXP1), b) A simulation that takes into account the current feedback into the estimation of the surface stress but neglects the atmospheric response (*e.g.*, EXP2), and c) A fully coupled simulation, *i.e.*, that has the current feedback into the surface stress estimate and the atmospheric response (*e.g.*, EXP3). In EXP1 (*i.e.*, simulations without current feedback), the net $F_e K_e$ is equal to zero. In EXP2 (*i.e.*, simulations with current feedback to the surface stress), over an eddy, the amount of positive wind work ($F_e K_e$) is reduced and the amount of negative $F_e K_e$ becomes more negative. As a result, the net $F_e K_e$ becomes negative, deflecting energy out of the eddy to the atmosphere. In a fully coupled model (EXP3), the atmospheric response damps the sink of $F_e K_e$ by increasing the positive $F_e K_e$ and decreasing the negative $F_e K_e$, the net $F_e K_e$ remaining negative. The current feedback induces a positive (negative) stress curl (wind curl) in the eddy's center.

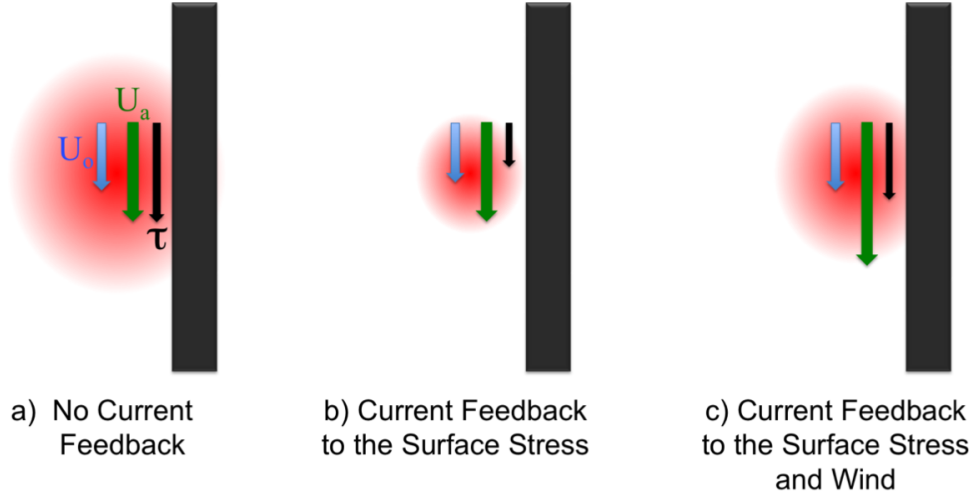


FIG. 6. Schematic representation of the current feedback considering a uniform southward wind blowing along the coast. a) A simulation without current feedback (*e.g.*, EXP1), b) A simulation that takes into account the current feedback into the estimation of the surface stress but neglects the atmospheric response (*e.g.*, EXP2), and c) A fully coupled simulation, *i.e.*, that has the current feedback into the stress estimate and the atmospheric response (*e.g.*, EXP3). The green, black, and blue arrows represent the wind, surface stress, and oceanic surface current, respectively. The red shade represents the induced $F_e K_e$ (positive in all cases). The wind induces an oceanic coastal geostrophic jet that is partially in the same as direction than the wind, inducing a positive $F_e K_e$. From EXP1 to EXP2, the reduction of the stress induces in turn a weakening of $F_e K_e$. From EXP2 to EXP3, the wind accelerates, increasing back toward its initial value the surface stress and hence $F_e K_e$ and the oceanic coastal geostrophic jet.

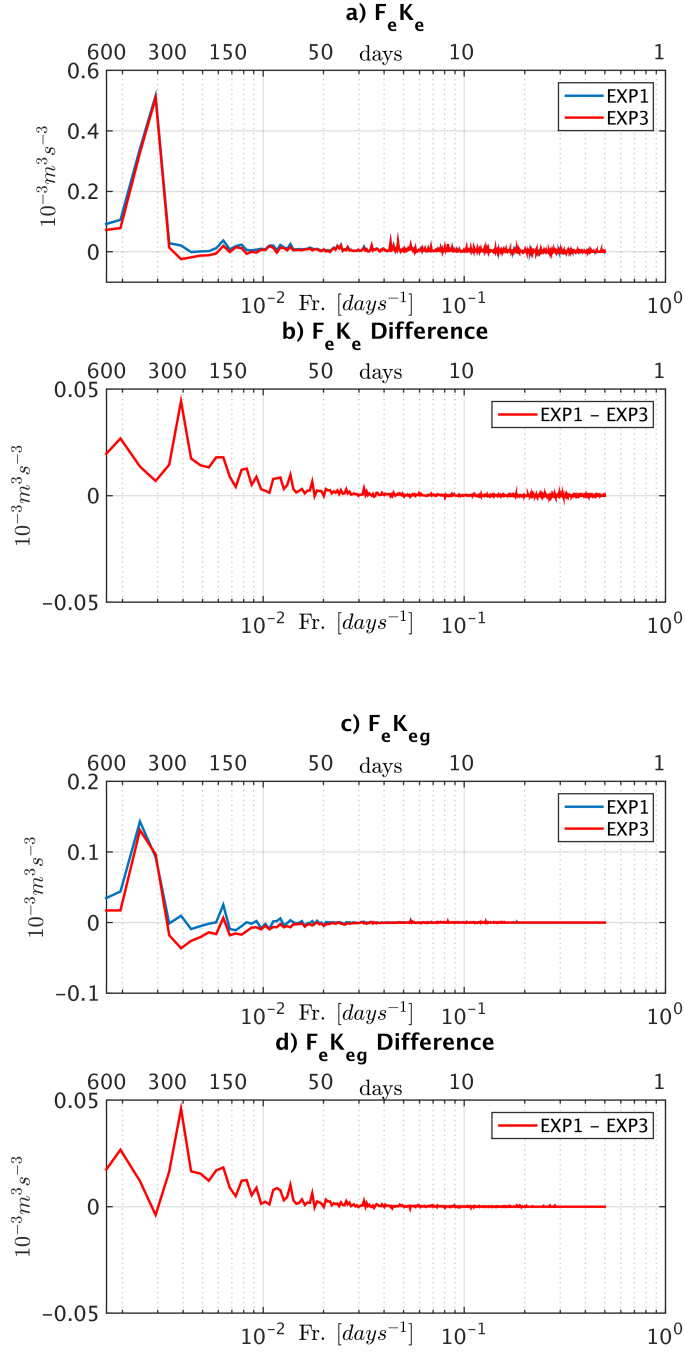


FIG. 7. a) Temporal 1D co-spectrum of the total wind work FK from EXP1 and EXP3 between 30°N and 45°N for the offshore region ($d > 80 km$), b) Difference between EXP1 and EXP3. c) Same than (a) but for the geostrophic wind work, d) same as b) for the geostrophic wind work. The current feedback to the atmosphere act as an eddy killer by reducing $F_e K_e$ through its geostrophic component, deflecting energy from the ocean to the atmosphere.

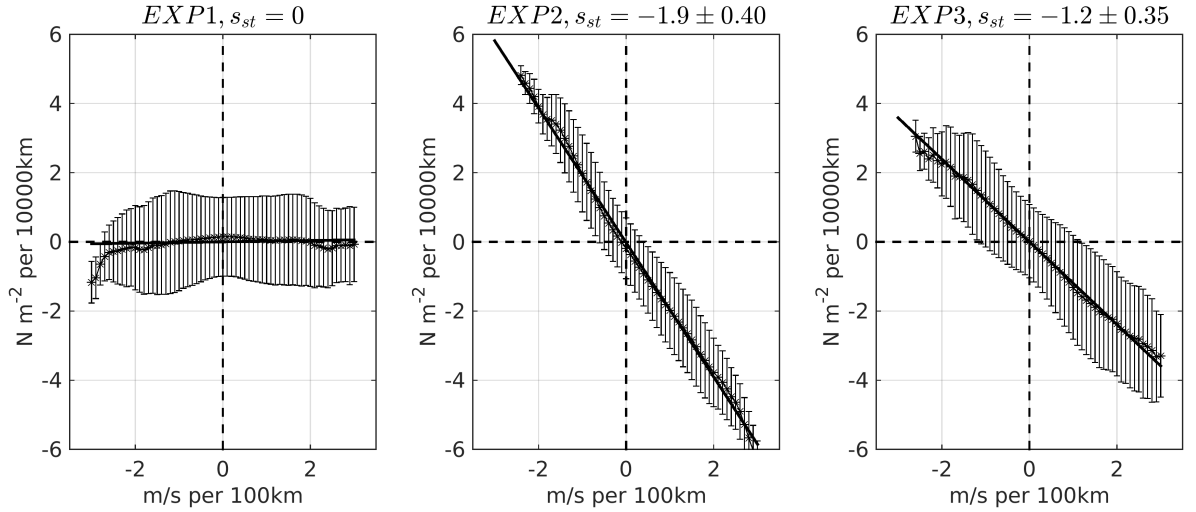


FIG. 8. Binned scatterplot of the full time series of 1-month running means of surface stress curl and surface current vorticity over the domain $30^\circ\text{N} - 45^\circ\text{N}$ and $(150\text{ km} < d < 500\text{ km})$. The bars indicate plus and minus one the standard deviation about the average drawn by stars. The linear regression is indicated by a black line and the slope s_{st} is indicated in the title ($10^{-2} N s m^{-3}$). From the left to the right: EXP1, EXP2, and EXP3. EXP1 does not have a significant slope since it does not have the current feedback to the atmosphere nor the surface stress. EXP2 and EXP3 presents a clear negative linear relationship between the currents and the stress curl. The currents feedback induce fine scale wind stress structure. Consistently with the previous results, the atmospheric response reduces the current feedback effect on the stress.

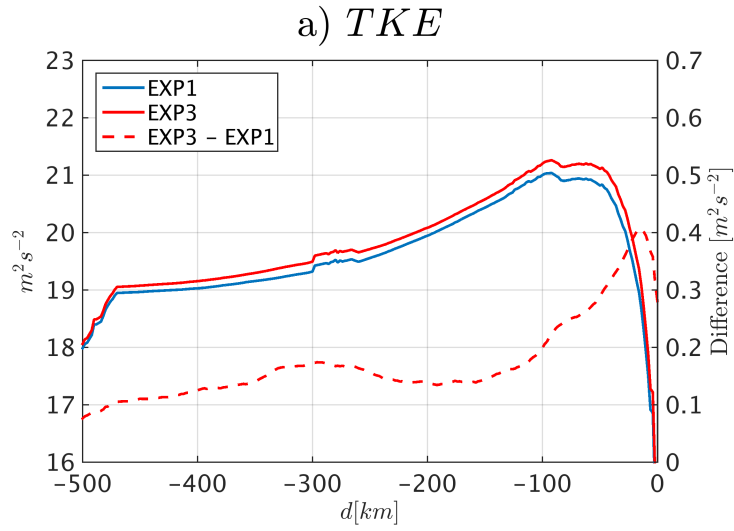


FIG. 9. a) Cross-shore profile of the Turbulent Kinetic Energy (TKE) of the surface wind averaged between 30°N and 45°N from EXP1 (cyan) and EXP3 (red). The $F_e K_e$ sink from the ocean to the atmosphere results in a slightly larger TKE in EXP3 compared to EXP1. In the nearshore region, there is a larger wind enhancement that is likely partly explained by the presence of the steady oceanic geostrophic jet that flows in the same direction as the wind.

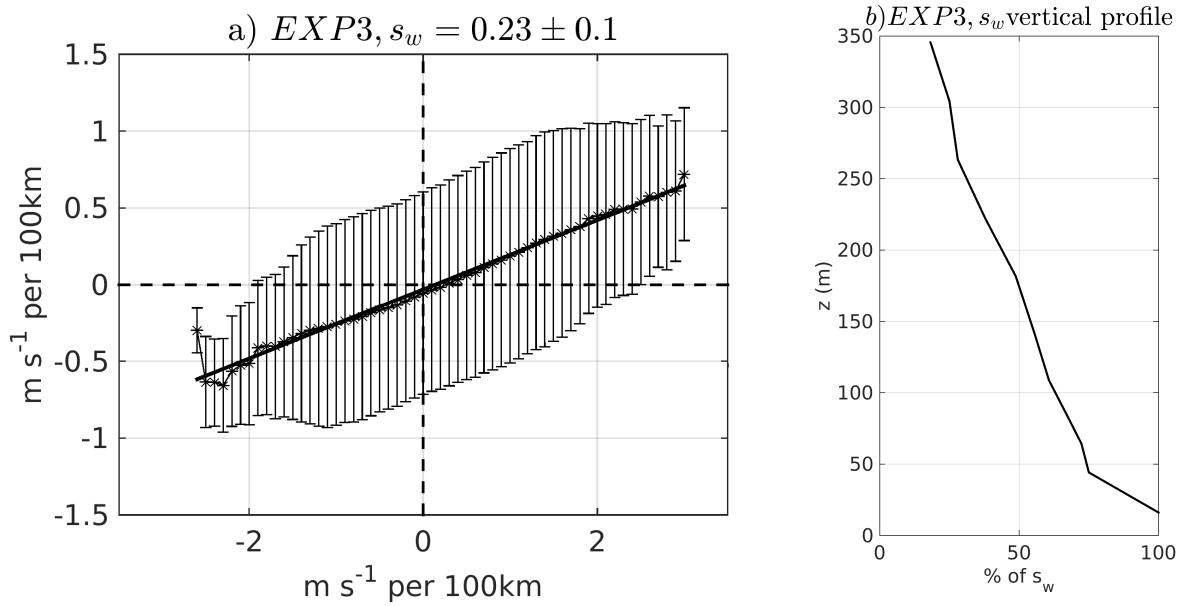


FIG. 10. a) Same as Fig. 8 but for the wind curl and the surface current vorticity for EXP3. There is a positive linear relationship between the current vorticity and the wind curl, *i.e.*, the current feedback on the atmosphere induces fine scale structures in the wind field that counteract the current-induced stress structure (Fig. 8). This explains the damping of the current feedback effect on the EKE (see text). The linear regression is indicated by a black line and the dimensionless slope s_w is indicated in the title. b) Vertical attenuation of s_w with respect to the surface s_w .

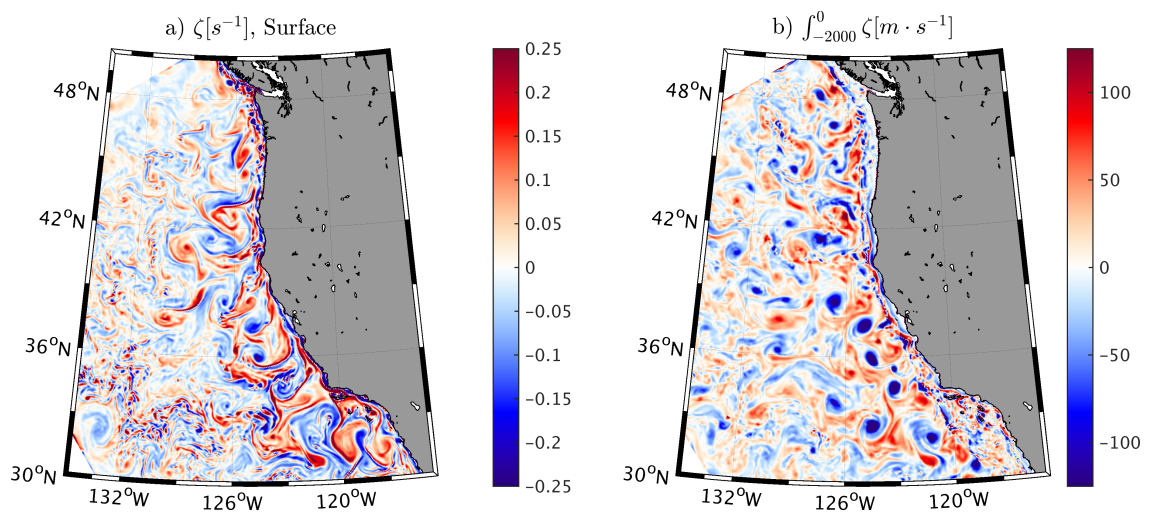


FIG. 11. a) Snapshot of sea surface relative vorticity and b) 2000 m integrated relative vorticity, from EXP3. The colorbar scale is adjusted between (a) and (b) by a factor of $D = 500$ that allows to have a rough match between the two panels. D factor is interpreted as the characteristic vertical scale of the eddies.

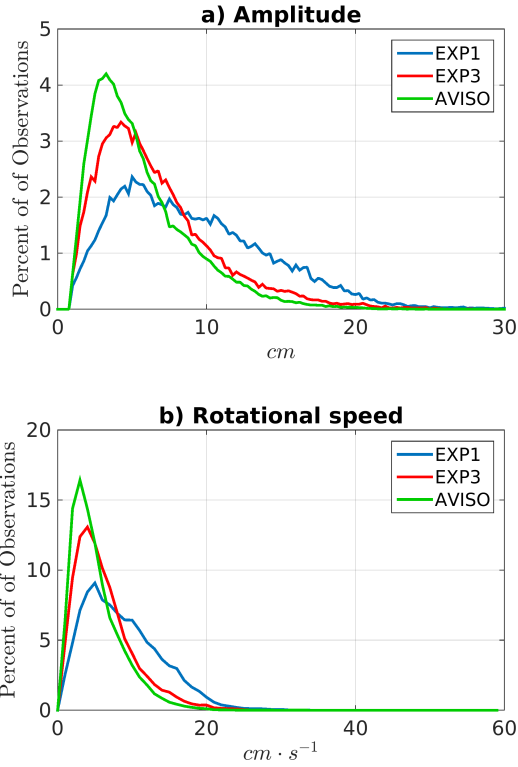


FIG. 12. Long-lived (16 weeks) eddy amplitude and rotational speed statistics from EXP1 (blue), EXP3 (red), and AVISO (green). Consistently with the previous results, the current feedback to the atmosphere damps the eddy amplitude and rotational speed, improving the realism of the simulation.

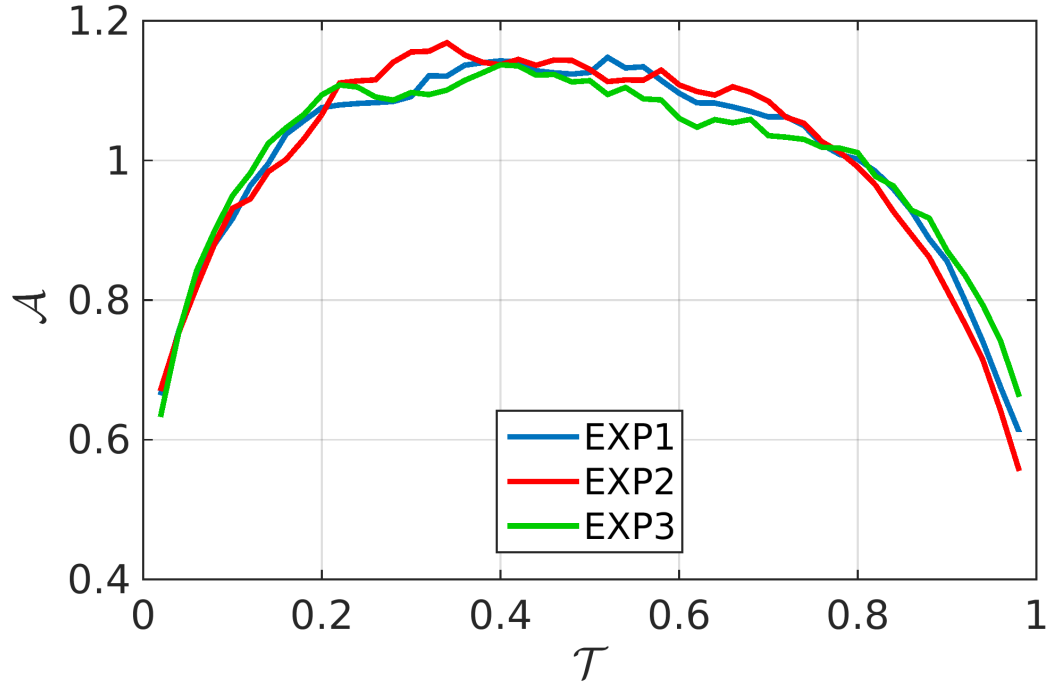


FIG. 13. Evolution of eddy normalized amplitude \mathcal{A} as a function of their dimensionless time \mathcal{T} for all tracked eddies with a lifetime greater than 16 weeks. The blue, red, and green colors represent the results from EXP1, EXP3, and AVISO. In EXP3, consistently with AVISO, the eddy first grows in size, then, due to the current feedback to the atmosphere, decreases slowly, and finally, decreases rapidly before collapsing. In EXP1, the slow decrease is not evident.

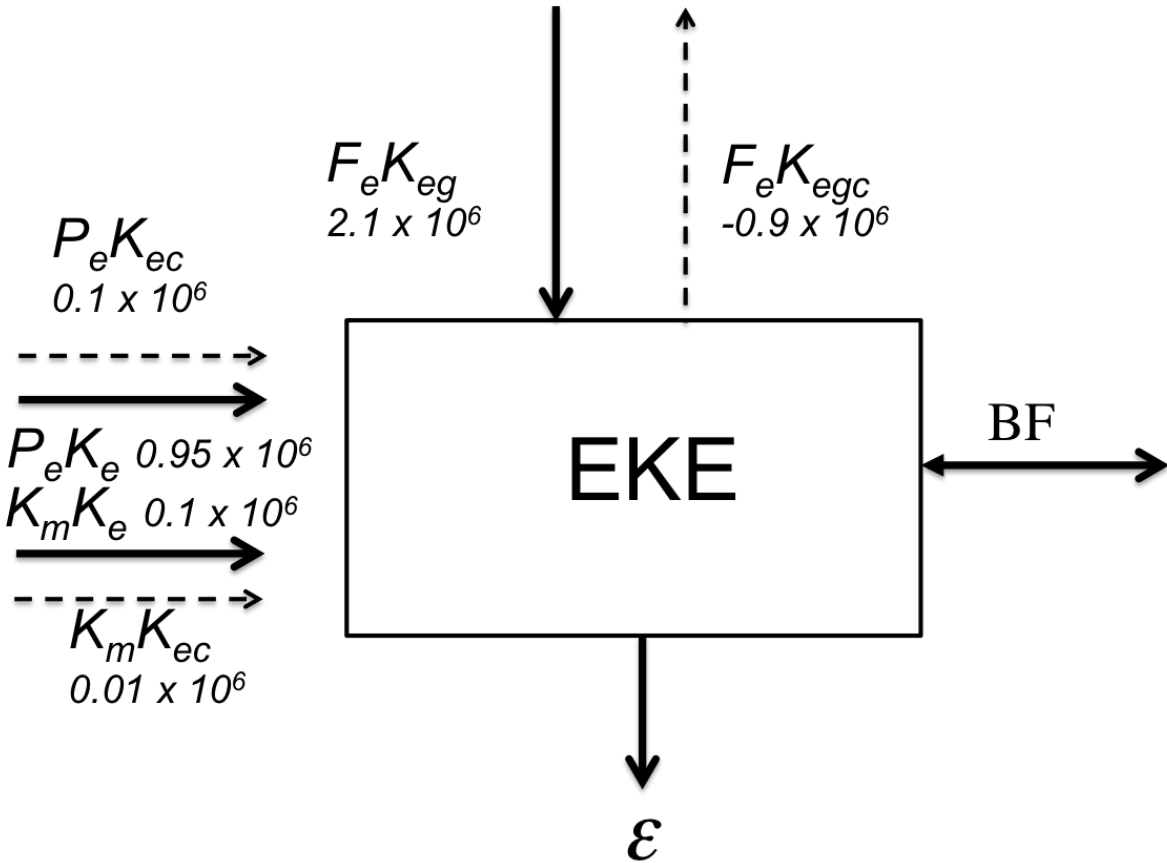


FIG. 14. An expanded Lorenz diagram of energy conversion for the depth-integrated EKE, integrated over the whole U.S. West Coast domain for the period 1995-1999. The atmosphere is above and mean ocean KE and PE to the left (not represented). The current feedback to the atmosphere mainly removes energy from the ocean to the atmosphere through the geostrophic flow. The mean integrated values for each conversion term are indicated in $m^5 s^{-3}$. ϵ is the dissipation term, and BF the energy flux o through the boundary. See text for more information.